JOURNAL OF PETROLOGY | VOLUME 54 | NUMBER 6 | PAGES 1109–1148 | 2013 | doi:10.1093/petrology/egt007

The Evolution of the Peach Spring Giant Magma Body: Evidence from Accessory Mineral Textures and Compositions, Bulk Pumice and Glass Geochemistry, and Rhyolite-MELTS Modeling

AYLA S. PAMUKCU[1]*, TAMARA L. CARLEY[1], GUILHERME A. R. GUALDA[1], CALVIN F. MILLER[1] AND CHARLES A. FERGUSON[2]

[1]DEPARTMENT OF EARTH & ENVIRONMENTAL SCIENCES, VANDERBILT UNIVERSITY, NASHVILLE, TN 37240 USA
[2]ARIZONA GEOLOGICAL SURVEY, TUCSON, AZ 84719, USA

RECEIVED AUGUST 26, 2011; ACCEPTED JANUARY 15, 2013
ADVANCE ACCESS PUBLICATION FEBRUARY 26, 2013

The Miocene Peach Spring Tuff is a giant (≥640 km^3 dense rock equivalent) pyroclastic deposit that is extensively exposed in the southwestern USA. Evidence from geochemical and textural analyses of bulk-rocks, glasses, and accessory minerals (zircon, titanite, allanite, chevkinite, magnetite) from outflow and intra-caldera pumice clasts and fiamme, in combination with field observations and rhyolite-MELTS modeling, suggests that the Peach Spring magma body was compositionally and thermally zoned with a basal cumulate, and that it crystallized over millennial timescales before being remobilized by mafic input prior to erupting. Crystal contents, bulk compositions, spatial distributions, and temperatures (recorded by Ti in zircon and Zr in titanite) of pumice clasts and fiamme vary systematically: distal outflow high-silica rhyolites are crystal-poor and document lower temperatures; intra-caldera trachytes are crystal-rich and record higher temperatures. These variations indicate that the Peach Spring magma body was zoned. We interpret the outflow high-silica rhyolites to represent the first portion of the magma body to erupt. Zircon and titanite display core-to-edge reductions in rare earth element (REE) concentration and temperature, suggestive of relatively uninterrupted crystallization as the magma body cooled; crystallization temperature intervals from rhyolite-MELTS are consistent with those recorded by zircon and titanite. Exponential size distributions for accessory minerals and phenocryst textures are consistent with geochemical evidence for a simple cooling and crystallization history. Intra-caldera trachytes and outflow low-silica rhyolites represent the later portion of the magma body to erupt. This magma experienced a late-stage heating event potentially associated with the onset of the eruption. The edges of titanite crystals are enriched in REE and Zr, and zircon edges are enriched in Ti, suggesting higher temperatures during edge crystallization (at least 900°C). Concave-down crystal size distributions and resorption features on phenocrysts are additional signs of heating. Rare trachyandesite enclaves and the presence of mafic to intermediate lavas immediately underlying the Peach Spring Tuff suggest that a mafic magma input may have been the cause of the heating. Evidence further suggests that the intra-caldera trachytes may represent a remobilized cumulate at the base of the magma body, which retained some melt prior to rejuvenation. Bulk pumice and fiamme compositions are very rich in feldspar and accessory mineral phenocrysts, indicative of accumulation of these minerals; high crystal contents (≥35%) and evidence of heating and resorption imply that this magma was even more crystal-rich prior to the heating event. Rhyolite-MELTS simulations suggest that the trachyte magma had roughly 1wt % water, which cannot be totally accounted for by hydrous phases, thus requiring some amount of melt within the cumulate. Kinked magnetite size distributions are interpreted to represent a change from growth-dominated crystallization (larger crystals, shallow slopes) to nucleation-dominated (small crystals, steep slopes) owing to the onset of eruptive decompression. Timescales of magnetite crystallization calculated from these slopes indicate that the Peach Spring magma body crystallized over millennial timescales, and that eruptive decompression began 10^{-1}–10^2 years prior to eruption.

*Corresponding author. E-mail: ayla.s.pamukcu@vanderbilt.edu

Timescales of zircon crystallization are consistent with those obtained from magnetite and suggest that much of the zircon growth in the Peach Spring magma body occurred simultaneously with the growth of the other phenocrysts.

KEY WORDS: *crystal size distribution; cumulate; geothermometry; ignimbrite; mineral chemistry; rejeuvination; rhyolite-MELTS; geochemistry*

INTRODUCTION

The ignimbrites that result from 'super-eruptions' provide striking evidence that large (100 to $\geq$1000 km^3) magma reservoirs exist within the Earth's crust (see Wark & Miller, 2008, and references therein). Studying these ignimbrites can provide important insight into the evolution of such large magma bodies, including their longevity and the mechanisms that may trigger a super-eruption. On a broader scale, such studies serve to clarify how and why super-eruptions are (or are not) comparable with eruptions of lesser magma volumes and to what extent these giant systems are similar to those that form large batholiths.

Some ignimbrites display a wide spectrum of compositions (from dacite to rhyolite; e.g. Upper Bandelier Tuff, Smith & Bailey, 1966; Youngest Toba Tuff, Chesner & Rose, 1991) and are typically characterized by an inverse correlation in crystal fraction and bulk silica content. These systematic variations in composition and crystallinity are often also reflected in their stratigraphic position, which has been interpreted as reflecting zonation of the magma body prior to eruption (e.g. Smith, 1960, 1979; Lipman *et al.*, 1966; Hildreth, 1981; Bachmann & Bergantz, 2004). At the other end of the spectrum are ignimbrites that show little to no evidence for bulk compositional zonation. Some ignimbrites in this category are crystal-rich, intermediate in composition and have been suggested to be remobilized crystal mushes (e.g. Fish Canyon Tuff, Bachmann & Bergantz, 2004; Lund Tuff, Maughan *et al.*, 2002; Altiplano–Puna Volcanic Complex, De Silva *et al.*, 1994). Others are crystal-poor, high-silica rhyolite (75–77 wt % SiO_2, Hildreth, 1981) in composition (e.g. Bishop Tuff, Hildreth, 1979) and have been suggested to represent melts extracted from crystal cumulates (Bachmann & Bergantz, 2004; Hildreth, 2004).

Mafic magma injection has been implicated as important in the development of large magma bodies and as a potential eruption trigger (e.g. Sparks *et al.*, 1977; Pallister *et al.*, 1992; Bachmann & Bergantz, 2003; Bindeman & Valley, 2003; Kennedy & Stix, 2007; Wark *et al.*, 2007; Deering *et al.*, 2011). Such injections are important sources of heat and volatiles and may lead to overpressurization and eruption of a system (Sparks *et al.*, 1977; Pallister *et al.*, 1992). Mafic magma injection may also play a role in creating the gradients in composition and crystal fraction that are observed in some large ignimbrites, by releasing silica-rich, crystal-poor, interstitial melt from a crystal mush through gas-driven filter pressing (Sisson & Bacon, 1999).

The longevity of large magma bodies in the Earth's shallow crust is a provocative issue that has sparked considerable debate. The results of isotopic studies have been inconsistent, with some suggesting long residence times ($\geq 10^2$ kyr; e.g. Halliday *et al.*, 1989; Bindeman & Valley, 2002; Vazquez & Reid, 2004; Simon & Reid, 2005) and others implying much shorter timescales (of the order of 1 kyr; e.g. Crowley *et al.*, 2007). Recent work on the Bishop Tuff, based on crystal size distributions, Ti zoning profiles in quartz, melt inclusion faceting, and heat flow modeling, suggests that these large magma bodies may be relatively ephemeral features with lifetimes on the scale of millennia (Gualda *et al.*, 2012*b*; Pamukcu *et al.*, 2012).

The Peach Spring Tuff, a large volume, early Miocene ignimbrite in the southwestern USA (Fig. 1), records the evolution of a giant magmatic system preserved in its extensive outflow sheet deposits (Young & Brennan, 1974; Buesch & Valentine, 1986; Glazner *et al.*, 1986) and a recently identified source caldera—the Silver Creek caldera, Arizona (Pearthree *et al.*, 2009; Ferguson *et al.*, 2012). The accessory minerals of the Peach Spring Tuff, particularly zircon, titanite, allanite, and a chevkinite-group phase, are major reservoirs of trace elements, notably U, Th, and REE (rare earth elements), making them useful as geochronometers, geothermometers, and monitors of magmatic trends. As such, they can be used to place constraints on conditions in and during the evolution of the Peach Spring magma body; thus, they may provide important insight into the evolution and eruption of giant silicic systems.

In this study, we combine information contained in the textures and compositions of accessory minerals, bulk-rocks, and glasses of Peach Spring pumice clasts and fiamme with the results of rhyolite-MELTS (Gualda *et al.*, 2012*a*) simulations. We have qualitatively and quantitatively studied textures by thin-section analysis, as well as by conventional and differential absorption X-ray tomography; analyzed accessory minerals by ion microprobe microanalysis; and determined the elemental compositions of glasses by electron microprobe and laser ablation inductively coupled plasma mass spectrometry (LA-ICP-MS) microanalysis. Our data provide substantial information on the compositional evolution of the Peach Spring magma preceding its eruption that may be applicable to other giant magma bodies. More broadly, our dataset shows the benefit of integrating geochemical, textural, and modeling-based data in the study of volcanic systems of all sizes.

GEOLOGICAL BACKGROUND

The Peach Spring Tuff (formerly Peach Springs Tuff; see Billingsley *et al.*, 1999) is a large, early Miocene ignimbrite

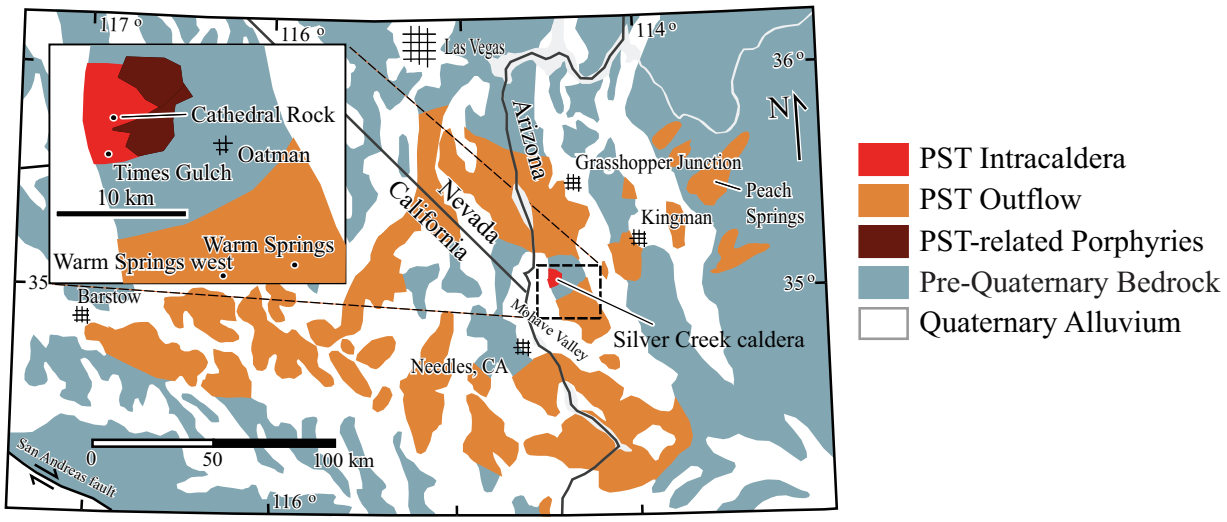

Fig. 1. Map showing the location of the Silver Creek caldera and areas from which the Peach Spring Tuff has been reported; modified from Wells & Hillhouse (1989). Inset map shows the locations discussed in the text in relation to the caldera complex, which includes related porphyries (Ferguson *et al.*, 2012). The intra-caldera deposits mark the exposed caldera, and the PST-related porphyries were emplaced near the caldera margin.

located in the southwestern USA. It was first defined by Young & Brennan (1974), who used it to study the geomorphological evolution of the southwestern edge of the western Colorado Plateau. Glazner *et al.* (1986) broadened its known extent to the Mojave Desert, where field observations and phenocryst assemblages were used to correlate tuff outcrops with the Peach Spring Tuff. It has since been mapped and described extensively (e.g. Wells & Hillhouse, 1989; Sherrod & Neilson, 1993) around the border of Arizona, Nevada, and California (Fig. 1). Buesch (1992) estimated that the Peach Spring outflow sheet covered an area of at least 32 000 km^2 and had a volume $\geq$640 km^3 dense rock equivalent.

The Peach Spring Tuff represents a geologically instantaneous eruptive event that occurred within a period of significant regional extension (Howard & John, 1987). Sanidine crystals in the Peach Spring Tuff dated by Ar/Ar have been reported to have an age of 18·5 ± 0·2 Ma (Nielson *et al.*, 1990; Miller *et al.*, 1998), but a more precise revised age of 18·78 ± 0·02 Ma (using the 28·20 Ma age for the Fish Canyon sanidine standard; see Kuiper *et al.*, 2008) has recently been reported (Ferguson *et al.*, 2012). Originally, the Peach Spring Tuff was thought to record a single cooling unit (e.g. Young & Brennan, 1974; Glazner *et al.*, 1986; Buesch, 1992). However, recently it has been proposed that it may include two cooling units in some locations (Varga *et al.*, 2004); nevertheless, if multiple cooling units do exist their contacts are subtle, and they are unlikely to represent time breaks of more than about a month (D. Buesch, personal communication).

The Peach Spring Tuff is typically strongly welded and varies in thickness from 10–15 m or less in distal portions (e.g. Barstow, California) to 60–140 m in more proximal localities (e.g. Kingman, Arizona; Piute Mountains, California) (Glazner *et al.*, 1986). Although Young & Brennan (1974) initially described the Peach Spring Tuff as trachytic, subsequent investigations of the major element geochemistry of pumice clasts in the outflow indicate that it is rhyolitic in composition (Gaudio, 2003; Carley, 2010; this study). The Peach Spring outflow contains 4–14% phenocrysts (Young & Brennan, 1974) of primarily feldspar (sanidine ≫ plagioclase), biotite, hornblende, pyroxene, and rare quartz. Accessory minerals include common titanite, zircon and allanite, as well as a chevkinite-group phase, apatite, and opaque oxides (primarily magnetite).

Given the volume of the Peach Spring Tuff, it is expected that a sizeable caldera (15–20 km diameter; Smith, 1979) would have been produced from its eruption; however, despite concerted efforts by numerous workers in the Black (Arizona) and Newberry (Nevada) Mountains (Young & Brennan, 1974; Glazner *et al.*, 1986; Hillhouse & Wells, 1991; Buesch, 1992), the precise location of the Peach Spring source was unknown until recently. New detailed mapping has significantly revised the stratigraphic sequence in the Black Mountains, resulting in the suggestion by Ferguson (2008) that the interior of the Alcyon Caldera, identified in the Black Mountains by Thorson (1971), might be the source caldera for the Peach Spring Tuff. Further study of a thick trachyte ignimbrite in the interior of this caldera indicated an age and phenocryst population nearly identical to that of the distinctive Peach Spring Tuff outflow sheet (corroborated by this study). As a result, this caldera, now known as the Silver Creek caldera based on the location of its principal known exposure near Oatman, Arizona, is thought to be the Peach Spring source caldera (Ferguson *et al.*, 2012). The volume of

caldera fill in the ~10 km diameter preserved fragment at Silver Creek, plus another ~10 km^2, ~1 km thick fragment near Eagle Peak, California, increases the known volume of eruption products by at least 60 km^3 to ~700 km^3 (Ferguson *et al.*, 2012).

MATERIALS AND METHODS

Our primary goal was to study the history and evolution of the Peach Spring magmatic system as recorded by the compositions and textures of glasses and phenocrysts, particularly of the relatively abundant accessory mineral phases. We combined major and trace element analyses on bulk pumice and fiamme, glasses, and phenocrysts with data on textural features, and we used rhyolite-MELTS modeling to better understand the conditions of crystallization in the Peach Spring magma body. For this thermodynamic modeling we ran simulations using two bulk compositions, each described by a bulk analysis of a sample representing a compositional end-member of the Peach Spring magmatic system.

We focused on four accessory mineral phases: zircon [$(Zr,Hf)SiO_4$], titanite [$(Ca,REE)_4TiSiO_5$], allanite [$(Ca,REE)_2(Al,Fe)_3(SiO_4)_3(OH)$], and chevkinite [$(Ca,REE)_2(Ti,Fe)_3Ti_2Si_4O_{22}$]; we refer to La–Pm as light REE (LREE), Sm–Dy as middle REE (MREE), and Ho–Lu as heavy REE (HREE). Magnetite textures were also studied. We have positively identified both allanite and chevkinite in these samples; however, they cannot be distinguished from each other by X-ray tomography, and they are generally so small and uncommon in thin section that they are difficult to distinguish optically. Thus, we have characterized these minerals together as allanite + chevkinite. No attempt was made to distinguish between the two most common members of the chevkinite group, chevkinite and perrierite, which can be done only by X-ray diffraction (Macdonald & Belkin, 2002), and we refer to them as chevkinite for convenience.

Methods overview

Textures and trace element compositions of accessory minerals and glasses in outflow and intra-caldera pumice clasts and fiamme were characterized using a number of techniques; the reader is referred to Supplementary Data Electronic Appendix 1 (available for downloading at http://www.petrology.oxfordjournals.org) for more detailed discussion of the analytical methods, operating procedures, and analytical errors, which are only briefly described here. Additional information was collected on bulk-rock geochemistry, bulk densities, and phenocryst assemblages of pumice and fiamme samples. Bulk pumice and fiamme determinations were conducted at ACTLABS (Ontario, Canada) by ICP-MS and instrumental neutron activation analysis (INAA). Bulk densities of samples were measured using an immersion method described by Gualda *et al.* (2004). Phenocryst assemblages were determined by optical microscopy of thin sections and, where possible, X-ray tomography and electron microscopy.

Textures were quantitatively and qualitatively analyzed using three methods, as follows.

(1) Conventional and differential absorption X-ray tomography were used to analyze the textures of zircon, titanite, allanite + chevkinite, and magnetite, following methods outlined by Gualda & Rivers (2006), Gualda *et al.* (2010) and Pamukcu & Gualda (2010). Conventional tomography results in maps of linear attenuation coefficient, whereas differential absorption tomography provides element-specific maps for high-Z elements, most notably Zr and REE. Differential absorption tomography was used to assess zircon (using Zr maps) and allanite + chevkinite (using Ce maps) textures and crystal size distributions, whereas conventional tomography was used to document titanite and magnetite textures and crystal size distributions (using contrast in mean atomic number).
(2) Optical and electron microscopy of thin sections was carried out.
(3) Handpicked crystal separates were studied.

Trace element compositions of glasses were determined by LA-ICP-MS, using a New Wave 213 nm laser attached to a Perkin–Elmer ELAN 6100 DRCII quadrupole ICP-MS system, with 60 μm laser spots and He as a carrier gas (see Supplementary Data Electronic Appendix 1). A significant number of glass analyses were excluded owing to extensive alteration of the glass or presence of microlites, identified by monitoring intrasample variability of elemental concentrations, particularly REE patterns (e.g. positive Eu anomalies indicative of feldspar inclusions). We did not determine major element compositions of glasses in this study, but electron microprobe data on major element concentrations in glass from a single Peach Spring outflow high-silica rhyolite pumice clast (KPST01D) have been given by Colombini *et al.* (2011). Reverse geometry sensitive high-resolution ion microprobe (SHRIMP-RG) was used to determine the compositions of zircon and titanite crystals using the basic operating parameters and trace element routines described by Mazdab *et al.* (2007), Mazdab (2009) and Claiborne *et al.* (2010).

Thermodynamic and geochemical modeling of the Peach Spring magma was conducted using rhyolite-MELTS (Gualda *et al.*, 2012*a*), a modified calibration of MELTS (Ghiorso & Sack, 1995) adjusted to better compute the quartz–feldspar saturation surface as a function of pressure for silicic systems. The simulations presented here are not aimed at modeling in detail the evolution of the Peach Spring magma body, but rather are used to derive information on: (1) crystallization and melting temperature intervals that can be compared with information

derived from thermobarometry; (2) sensible and latent heat contributions to crystallization and melting and, in particular, the enthalpy versus temperature evolution; (3) titania and silica activities to be used with Ti-in-zircon and Zr-in-titanite thermometry. We have used two end-member compositions: a crystal-poor high-silica rhyolite from the outflow sheet (KPST01D, ~75 wt % SiO_2), and an intra-caldera crystal-rich trachyte (CRW, ~66 wt % SiO_2). Isobaric simulations were run with variable initial water contents between 0·25 and 7 wt % to explore a wide range of fluid saturation conditions. The crystallization pressure of the Peach Spring pumice and fiamme is constrained to be between 200 and 300 MPa considering the coexistence of two feldspars and glass, and the projection of glass compositions onto the Qz–Ab–Or ternary (Blundy & Cashman, 2001, 2008; see also Gualda *et al.*, 2012*a*), which is consistent with geological evidence for shallow-level crystallization; the effect of pressure on the parameters derived from rhyolite-MELTS used in this work is small, so we present only simulations at 250 MPa.

We employed data from SHRIMP-RG analyses to estimate temperatures during growth of zircon and titanite crystals, using the re-calibrated Ti-in-zircon thermometer (Ferry & Watson, 2007) and Zr-in-titanite thermobarometer (Hayden *et al.*, 2008). We estimated activities of titania (a_{TiO2}) and silica (a_{SiO2}) through the relationship $a = \exp(-A/RT)$, where A is the affinity of rutile or quartz, which can be retrieved from rhyolite-MELTS. Our results strongly favor crystallization of titanite under zircon-saturated conditions, so the activity of zircon (a_{ZrSiO4}) was assumed to be unity. We used a pressure of 250 MPa for titanite thermometry (see above); a ±50 MPa change in pressure results in a temperature difference of ~5–10°C, which can be neglected considering the uncertainties in titania and silica activities (see below).

Zircon saturation temperatures were calculated using both bulk pumice and glass compositions using the formulations of Watson & Harrison (1983). These formulations are based on the melt compositions (major elements and Zr concentrations) of zircon-saturated liquids. Therefore, estimated temperatures are strictly applicable for glasses, as zircon saturation is petrographically evident. These values should indicate the temperature at which zircon and melt last equilibrated, possibly near the time of eruption. For bulk pumice, the temperatures apply to a hypothetical melt with the bulk-rock composition. If zircon is relatively abundant in the phenocryst assemblage (mean Zr concentration is higher in phenocrysts than in melt), then the calculated temperature will exceed the temperature at the time of eruption; if zircon is absent from or under-represented in the phenocryst assemblage, the calculated temperature will be too low. Because zircon is ubiquitous and relatively abundant in pumice, bulk pumice temperatures are probably overestimates. Because most pumice is phenocryst-poor and so glass and pumice compositions are similar, we expect that the bulk pumice temperatures are high by no more than tens of degrees.

Samples

Samples were collected from locations representing different facies of the Peach Spring Tuff (Table 1, Fig. 1). Eleven samples were selected for detailed study: eight pumice clasts from the outflow sheet (KPST01A, 01B, 01C, 01D and 01E from Kingman; WSW2A and 2B from west of Warm Springs; GJ1A from Grasshopper Junction), two intra-caldera fiamme (PSTG01C from Times Gulch; CRW from west of Cathedral Rock) and a mafic enclave (WSW1). Bulk pumice and fiamme analyses, phenocryst assemblages, and some accessory mineral geochemistry for additional samples from the proximal outflow (WSW2C, 2D, 2E, 2F, 2G, 3A, 4B and 4D pumice clasts and fiamme from west of Warm Springs; GJ1A, 1B and 1C pumice clasts from Grasshopper Junction) are also included in the following discussion. All references to bulk analyses (e.g. bulk-rock composition, bulk density, etc.) correspond to single pumice clasts or fiamme. No bulk tuff samples have been analyzed as part of this study.

RESULTS

Bulk sample major element compositions

Pumice clasts and fiamme range substantially in bulk major element composition (Table 2, Figs 2 and 3); this compositional variability correlates with crystal content and proximity to the caldera. The relatively crystal-poor pumice clasts, collected from the more distal outflow (KPST01A, 01B, 01C, 01D and 01E) and parts of the proximal outflow (WSW2A, 2D, 2F and 2G), are high-silica rhyolite (74–76 wt % SiO_2, on an anhydrous basis). Low-silica rhyolite pumice clasts (71 wt % SiO_2) and fiamme (69–72 wt % SiO_2) have intermediate crystal contents and appear in the more proximal outflow (WSW2B, 4B and 4D). Crystal-rich fiamme from the proximal outflow Grasshopper Junction locality have compositions intermediate between these groups (72–73 wt % SiO_2). Fiamme from the intra-caldera fill are the most crystal-rich and are trachytic in composition (66–69 wt % SiO_2). The magmatic enclave (WSW1) is considerably more mafic in composition (57 wt % SiO_2; trachyandesite).

Most elements vary regularly as a function of SiO_2, with Al_2O_3, CaO, TiO_2, Fe_2O_3 (total Fe), MgO and P_2O_5 decreasing monotonically as SiO_2 increases (Fig. 3; see also Fig. 1 in Supplementary Data Electronic Appendix 2). Pumice and fiamme are characterized by very high K_2O (5·8–7·3 wt %), which remains relatively constant at all SiO_2 concentrations (Fig. 3). The trachyandesite enclave is not included on these plots, owing to its much lower silica content making the details of the primary sample set difficult to discern, but data for this sample are given in Table 2.

Table 1: Descriptions, locations, and analyses performed on samples used in this study

Sample name	Map location name	Location within tuff	Easting	Northing	Sample description	Analyses performed	Sample composition
KPST01A	Kingman	Distal outflow	0769890	3897793	Pumice clast	x, t, i, s	High-silica rhyolite
KPST01B	Kingman	Distal outflow	0769890	3897793	Pumice clast	x, t, i, s	High-silica rhyolite
KPST01C	Kingman	Distal outflow	0769890	3897793	Pumice clast	x, t, i, s	High-silica rhyolite
KPST01D	Kingman	Distal outflow	0769890	3897793	Pumice clast	x, t, i, s	High-silica rhyolite
KPST01E	Kingman	Distal outflow	0769890	3897793	Pumice clast	x, t, i, s	High-silica rhyolite
GJ1A	Grasshopper Junction	Distal outflow	0739361	3897793	Pumice clast	t, i, s	Low-silica rhyolite
GJ1B	Grasshopper Junction	Distal outflow	0739361	3897793	Pumice clast	t, i	–
GJ1C	Grasshopper Junction	Distal outflow	0739361	3897793	Pumice clast	t, i	Low-silica rhyolite
PT1B	Piute Mountains	Distal outflow	0670678	3848191	Fiamma	t	–
WSW1	Warm Springs West	Proximal outflow	0740155	3864385	Mafic enclave	t, i	Trachyandesite
WSW2A	Warm Springs West	Proximal outflow	0740155	3864007	Pumice clast	x, t, i, s	High-silica rhyolite
WSW2B	Warm Springs West	Proximal outflow	0740155	3864007	Pumice clast	x, t, i, s	Low-silica rhyolite
WSW2C	Warm Springs West	Proximal outflow	0740155	3864007	Pumice clast	x, t, i, s	–
WSW2D	Warm Springs West	Proximal outflow	0740155	3864007	Pumice clast	t, i	High-silica rhyolite
WSW2E	Warm Springs West	Proximal outflow	0740155	3864007	Pumice clast	i	High-silica rhyolite
WSW2F	Warm Springs West	Proximal outflow	0740155	3864007	Pumice clast	t	High-silica rhyolite
WSW2G	Warm Springs West	Proximal outflow	0740155	3864007	Pumice clast	t	High-silica rhyolite
WSW3A	Warm Springs West	Proximal outflow	0740405	3863908	Pumice clast	t	–
WSW4B	Warm Springs West	Proximal outflow	0740173	3864203	Fiamma	t, i	Low-silica rhyolite
WSW4D	Warm Springs West	Proximal outflow	0740173	3864203	Fiamma	t, i	Low-silica rhyolite
CRW	Cathedral Rock West	Intra-caldera	0731653	3882577	Fiamma	x, t, i, s	Trachyte
PSTG01C	Times Gulch	Intra-caldera	0730332	3881149	Fiamma	x, t, i, s	Trachyte

All waypoints are UTM zone 11S, NAD 27. All 'pumice clast' or 'fiamma' samples are a single pumice clast or fiamma. Whole-rock compositions have not been determined for those samples without a 'sample composition' designated. x, X-ray tomography; t, thin-section analysis; i, LA-ICP-MS; s, SHRIMP-RG.

Many of the other geochemical and textural data correlate well with these variations in major element geochemistry, location, and crystal content. Thus, for the sake of simplicity in subsequent discussion, the Peach Spring samples will be grouped together where possible. Silica content is a simple way to designate sub-groups; samples with $\geq$74 wt % SiO_2 will hereafter be referred to as 'high-silica rhyolite' (more distal KPST01A, 01B, 01C, 01D and 01E, referred to subsequently as KPST01A–E, and proximal WSW2A); samples with 69–73 wt % as 'low-silica rhyolite' (proximal WSW2B, 2F, 2G and GJ1A and 1C); and samples with <69 wt% as 'trachyte' (intra-caldera samples PSTG01C and CRW).

Bulk density determinations and phenocryst assemblages

The seven pumice clasts studied are relatively dense (1·14–1·59 g cm^{-3}; see Table 3); bulk densities of the more distal outflow high-silica rhyolite pumice clasts (KPST01A–E) cover a relatively wide range (1·14–1·41 g cm^{-3}), but they are somewhat lower than those of the high- and low-silica rhyolite pumice from the proximal outflow (WSW; 1·49–1·59 g cm^{-3}). Trachyte intra-caldera fiamme (PSTG01C and CRW) have much higher densities (2·53 g cm^{-3} and 2·57 g cm^{-3}, respectively). This trend probably reflects varying degrees of compaction and welding, in addition to composition.

Phenocryst assemblages of samples determined by optical microscopy and complemented by information from X-ray tomography and electron microscopy are summarized in Table 3. Quantitative abundances of phenocrysts have not been determined for these samples, but they are similar to what has been found in other portions of the Peach Spring Tuff (see Geological Background section): feldspar is much more abundant than the other mineral phases; sanidine is predominant over plagioclase, and quartz is rare or absent.

High- and low-silica rhyolite outflow pumice and fiamme samples contain feldspar (sanidine $\gg$ plagioclase, 2:1 to 5:1 ratio), zircon, titanite, magnetite $\pm$ ilmenite, and

Table 2: Bulk-rock geochemistry of outflow pumice clasts and fiamme, intra-caldera fiamme, and a mafic enclave

	KPST01A	KPST01B	KPST01C	KPST01D	KPST01E	WSW 2A	WSW 2B	WSW 2D	WSW 2F	WSW 2G
SiO_2	75·3	75·1	75·4	75·4	75·2	75·1	71·0	76·1	74·8	74·4
Al_2O_3	12·7	12·8	12·2	13·1	12·9	12·8	14·7	12·7	13·3	13·6
Fe_2O_3	1·19	1·17	1·09	1·06	1·18	1·40	1·96	1·09	1·27	1·32
MnO	0·08	0·07	0·07	0·07	0·07	0·08	0·08	0·05	0·04	0·05
MgO	0·17	0·26	0·35	0·20	0·24	0·20	0·23	0·09	0·13	0·12
CaO	1·13	0·61	1·15	0·75	1·02	0·61	0·85	0·51	0·60	0·65
Na_2O	2·23	2·63	2·62	2·72	2·29	3·64	4·04	3·29	3·45	3·56
K_2O	6·92	7·16	6·82	6·39	6·91	5·86	6·77	5·99	6·17	6·06
TiO_2	0·23	0·21	0·20	0·19	0·21	0·22	0·35	0·19	0·21	0·22
P_2O_5	0·02	0·02	0·03	0·03	0·02	0·02	0·02	0·02	0·02	0·02
Ba	32	51	34	40	48	40	75	70	60	65
Co	1·8	1·6	2·2	1·7	2·7	1·8	1·5	1·2	1·9	1·6
Cs	3·5	3·8	3·9	3·3	3·3	1·5	1·4	1·4	1·4	1·7
Cu	1	1	3	2	2	10	4	5	7	4
Ga	19	22	21	20	18	18	19	17	18	18
Hf	8·6	9·1	8·7	8·8	7·9	8·1	12·2	7·6	7·5	7·6
Nb	37·8	44·5	43·4	39·4	38·4	34·3	31	30·9	34	33·9
Pb	30	34	23	24	26	24	25	20	16	18
Rb	201	217	221	198	194	195	178	196	213	211
S	60	180	430	100	2830	60	40	120	150	70
Sc	3·63	3·42	3·43	3·48	3·59	3·63	3·58	2·71	3·15	3·31
Sr	17	14	17	17	18	18	23	21	26	19
Ta	2·50	2·80	2·80	2·50	2·50	2·43	2·18	2·23	2·33	2·53
Th	32·2	34·4	35·3	32·9	30·2	24·5	20·0	27·6	28·4	29·0
Tl	1·41	1·32	1·4	1·14	2·27	0·20	0·14	0·33	0·38	0·41
U	6·06	6·3	6·69	6·18	5·69	4·10	2·77	4·89	4·07	4·62
V	6	6	7	< 5	9	< 5	8	6	< 5	< 5
Y	38	36	33	33	38	33	57	33	32	33
Zn	50	58	52	50	37	46	55	27	36	39
Zr	221	239	223	221	200	257	513	249	252	238
La	70·1	72·1	68·8	69·7	69·0	78·3	115	75·3	69·1	78·2
Ce	127	131	124	124	121	141	231	127	117	136
Pr	14·7	15·2	13·9	13·9	14·5	15·6	30·0	14·4	13·2	15·1
Nd	42·2	43·4	38·6	38·7	41·7	48·2	107	43·9	41·8	45·1
Sm	7·82	7·93	6·81	6·72	7·52	8·50	22·3	8·01	7·35	8·01
Eu	0·58	0·64	0·51	0·57	0·58	0·63	1·55	0·60	0·59	0·63
Gd	6·51	6·62	5·66	5·51	6·48	6·48	15·9	6·08	5·45	6·53
Tb	1·06	1·08	0·91	0·89	1·02	1·03	2·63	0·99	0·91	1·01
Dy	6·07	6·17	5·44	5·20	5·71	5·85	14·0	5·66	5·21	5·62
Ho	1·17	1·19	1·07	1·03	1·10	1·19	2·49	1·12	1·08	1·15
Er	3·40	3·50	3·29	3·17	3·36	3·47	6·32	3·18	3·14	3·37
Tm	0·53	0·56	0·52	0·51	0·52	0·55	0·88	0·54	0·52	0·55
Yb	3·37	3·51	3·37	3·18	3·24	3·46	4·86	3·17	3·31	3·47
Lu	0·47	0·50	0·48	0·47	0·45	0·47	0·62	0·44	0·46	0·48
*M**	1·45	1·45	1·57	1·36	1·42	1·49	1·60	1·42	1·44	1·44
Zircon saturation *T* (°C)†	815	822	806	822	808	826	885	829	828	823

(continued)

Table 2: Continued.

	WSW 4B	WSW 4D	GJ1A	GJ1C	WSW1	PSTG01A	PSTG01C-1	PSTG01C-2	CRW
SiO_2	69·1	71·9	72·0	73·1	57·6	68·6	68·8	68·2	66·1
Al_2O_3	16·2	14·8	14·7	14·1	17·0	16·1	16·2	16·0	17·0
Fe_2O_3	1·98	1·69	1·83	1·80	7·48	2·32	2·24	2·74	3·26
MnO	0·05	0·05	0·04	0·08	0·07	0·07	0·07	0·08	0·06
MgO	0·60	0·35	0·17	0·19	2·50	0·48	0·43	0·46	0·81
CaO	1·19	0·92	0·56	0·61	5·41	1·39	1·29	1·26	1·21
Na_2O	3·75	3·86	3·89	3·74	3·50	4·15	4·00	3·91	3·50
K_2O	6·67	6·03	6·32	5·96	4·60	6·29	6·41	6·64	7·33
TiO_2	0·39	0·34	0·36	0·33	1·32	0·49	0·47	0·57	0·57
P_2O_5	0·04	0·03	0·06	0·06	0·55	0·11	0·10	0·10	0·20
Ba	222	59	87	209	1943	1066	1016	934	2850
Co	2·3	2·0	2·5	2·2	14·4	3·2	2·5	2·4	3·3
Cs	1·9	2·1	0·9	1·0	6·3	1·2	1·5	1·2	1·8
Cu	7	2	3	4	33	5	10	7	10
Ga	17	20	20	18	22	20	21	19	19
Hf	11·0	11·8	11·4	11·0	9·0	13·1	13·3	14·5	14·9
Nb	24·1	30·8	28·3	31·8	21·5	21·7	21·8	32·0	18·5
Pb	25	25	25	20	46	30	39	30	28
Rb	157	162	142	138	96	131	140	125	149
S	160	20	<10	180	350	20	80	30	20
Sc	5·30	3·28	3·22	3·31	12·2	6·55	6·05	6·77	7·36
Sr	67	27	22	37	1514	208	199	177	437
Ta	1·61	2·29	2·22	2·48	1·27	1·40	1·40	2·52	1·18
Th	19·0	20·8	22·2	20·6	20·3	19·4	19·8	21·1	16·7
Tl	0·12	0·24	0·32	0·33	0·54	0·65	0·78	0·24	0·45
U	2·53	2·91	2·82	2·50	4·15	3·83	4·11	3·27	2·39
V	12	9	19	12	109	21	16	23	32
Y	30	61	47	38	31	33	34	38	30
Zn	54	49	46	40	87	65	70	62	62
Zr	500	475	478	445	400	579	576	679	759
La	154	88·2	108	97·1	151	173	173	188	172
Ce	254	185	202	191	238	336	338	333	294
Pr	31·0	24·7	26·7	24·6	30·8	38·7	35·6	39·2	34·2
Nd	108	96·3	98·6	90·4	104	109	106	129	113
Sm	16·5	20·8	20·3	18·0	15·8	17·6	18·1	19·4	16·0
Eu	2·52	1·53	1·54	1·42	3·38	3·23	3·14	3·12	3·77
Gd	10·3	15·7	14·1	12·6	11·0	11·1	10·9	14·5	12·0
Tb	1·39	2·50	2·18	1·84	1·20	1·45	1·45	1·67	1·29
Dy	6·80	13·2	11·1	9·09	5·64	7·44	7·60	8·12	6·13
Ho	1·26	2·45	1·96	1·62	1·01	1·39	1·41	1·49	1·10
Er	3·43	6·16	4·88	4·06	2·74	3·89	3·93	4·04	3·08
Tm	0·50	0·85	0·73	0·58	0·37	0·55	0·57	0·58	0·42
Yb	3·02	4·79	3·83	3·42	2·35	3·32	3·49	3·53	2·72
Lu	0·45	0·60	0·51	0·45	0·33	0·50	0·50	0·50	0·40
*M**	1·49	1·46	1·44	1·42	2·23	1·58	1·53	1·57	1·52
Zircon saturation *T* (°C)†	892	889	891	886	808	899	903	918	935

Oxides are reported in wt % and normalized to 100% anhydrous; elemental concentrations are reported in ppm.

*M value calculated as $\frac{\text{mol(K+Na+2Ca)/total mol}}{\text{(mol Al/total mol)}\times\text{(mol Si/total mol)}}$.

†Zircon saturation temperatures calculated using Watson & Harrison (1983).

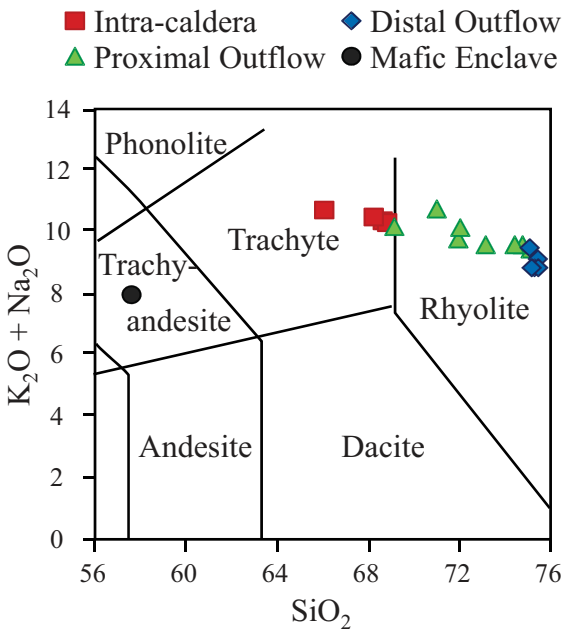

Fig. 2. Total alkalis vs silica diagram (in wt %) (after Le Bas *et al.*, 1986) used to classify the compositions of the outflow pumice and fiamme, intra-caldera fiamme, and a mafic enclave. The field that includes intra-caldera fiamme is labeled 'trachyte' because Q/QAPF < 0·2 (normative quartz is relatively low).

biotite (golden yellow to reddish brown pleochroism). Euhedral quartz was identified in the Kingman high-silica rhyolite (KPST01D), and subhedral to anhedral crystals (~250–400 μm) were found in WSW2D and GJ1B thin sections, showing that these melts were silica-saturated. Amphibole (golden yellow to dark brown pleochroism) is rare or absent in thin section, but we have identified it in the tomograms of all analyzed samples. Allanite ± chevkinite is found sparingly in some thin sections of both pumice and fiamme, but it is identifiable in tomograms of all analyzed pumice clasts. Apatite is not evident in thin sections from the outflow sheet, but it was found in some mounts using electron microscopy. Clinopyroxene is sparse in the WSW3A pumice clast and present as a single large crystal (~500 μm) in the WSW4B fiamma.

The trachyte fiamme contain sanidine, zircon, titanite, allanite ± chevkinite, magnetite ± ilmenite, amphibole, and biotite. Amphibole is typically present as fragments in thin section, but some euhedral to subhedral grains can be identified in tomograms. Biotite in both intra-caldera samples is commonly rimmed by, or entirely altered to, chlorite. CRW is distinct from all the other samples in that it contains an abundance of apatite, which is found readily in thin section and mounts.

The mafic enclave (WSW1) contains abundant clinopyroxene and sparse orthopyroxene. Plagioclase is the only feldspar present.

Bulk sample and glass trace element compositions

We obtained trace element data for all bulk pumice and fiamme detailed in this study and for glass from samples in which it was not recrystallized (KPST01A–E, high-silica rhyolite; CRW, trachyte; WSW1, mafic enclave) (Table 4; see Supplementary Data Appendix 1 for details). Trace element variations are plotted against Sr (Fig. 3), which serves as an indicator of differentiation in this feldspar-rich system. We emphasize Ba, Gd, Hf, La, Nd, and Yb as these elements strongly partition into zircon, titanite, allanite, chevkinite and sanidine, and can be used to elucidate crystallization and fractionation trends.

Concentrations of Ba, Gd, Hf, La, and Nd in glasses and bulk pumice and fiamme are positively correlated with Sr (Fig. 3, see also Fig. 2 in Supplementary Data Electronic Appendix 2), with high-silica rhyolite pumice clasts showing the lowest concentrations; bulk samples are enriched in these elements relative to glass. Glass in the mafic enclave (WSW1) is the most enriched in these elements, and bulk sample concentrations are typically depleted relative to glass. Yb remains nearly constant throughout the suite of samples.

Zircon saturation temperatures

Calculated zircon saturation temperatures (Tables 3 and 4) for high-silica rhyolite (KPST01B and D) glass are 770 and 780°C; bulk pumice (KPST01A–E; WSW2A, D, F, and G) yields temperatures in the range 810–830°C. Low-silica rhyolite bulk pumice (WSW2B, 4B and 4D; GJ1A and 1C) gives higher saturation temperatures of 880–890°C. Trachytes give considerably higher zircon saturation temperatures; glass in CRW yields a temperature of 920°C, and bulk fiamme (CRW and PSTG01) yield temperatures of 920 and 930°C.

The slightly higher calculated temperatures for bulk pumice and fiamme than for glass compositions are consistent with the presence of modest amounts of zircon in the phenocryst assemblages. The glass compositions suggest much lower eruption temperatures for high-silica rhyolite than for trachyte.

Zircon and titanite trace element composition

General trends in rare earth elements

REE data are typically displayed as chondrite-normalized plots; however, owing to the strong enrichment in HREE over LREE in zircon and in MREE over LREE and HREE in titanite (Fig. 4), such plots tend to hide subtle differences between analyses. To enhance these differences, we use REE plots normalized to an average zircon or titanite composition. We chose a zircon and a titanite analysis from one of the most evolved pumice samples (KPST01A). As typical for zircon, the average composition

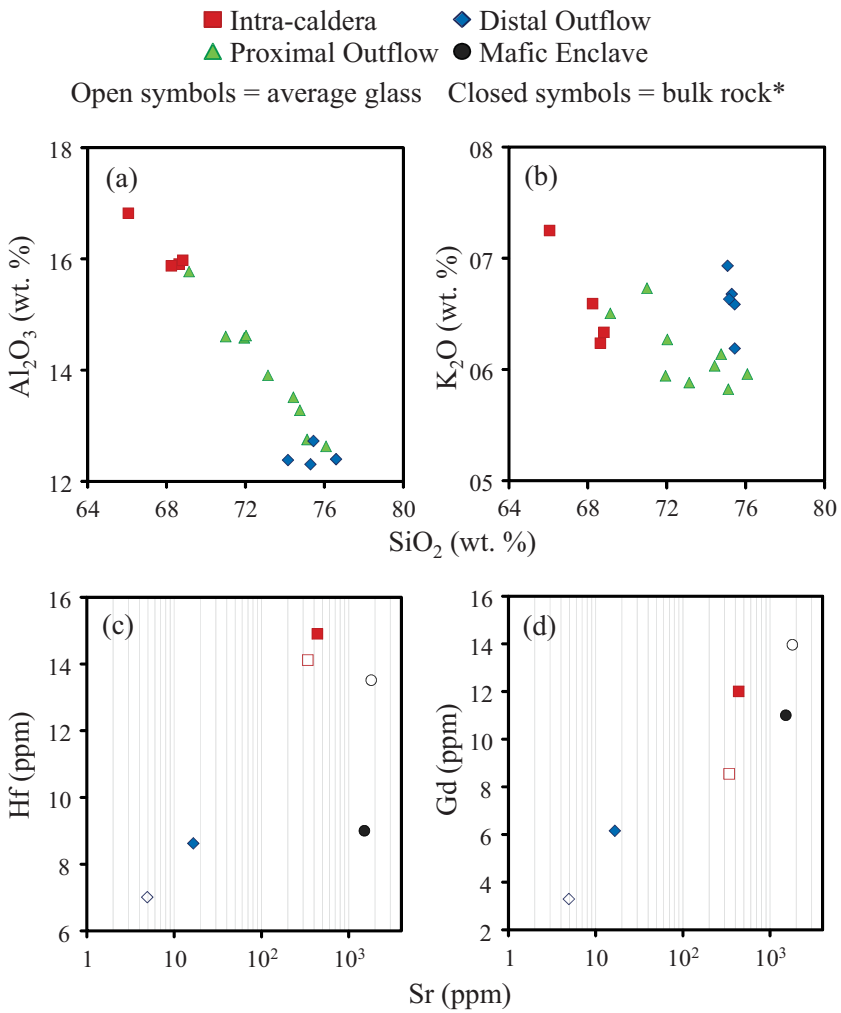

Fig. 3. Major and trace element variations in bulk pumice and fiamme (filled symbols) and glasses (open symbols). (a, b) Trends in SiO_2 vs Al_2O_3 and K_2O in bulk pumice clasts from the distal and proximal outflow, and fiamme from the intra-caldera and proximal outflow. Additional plots of major elements in the bulk pumice and fiamme can be found in Fig. 1 in Supplementary Data Electronic Appendix 2. Mafic enclave WSW1 (trachyandesite) is omitted from (a) and (b) to permit a clearer display of the variations in the more compositionally restricted pumice and fiamme. (c, d) Trends in Sr vs Hf and Gd in glasses and bulk-rocks for selected samples, including distal outflow pumice clasts (KPST01), an intra-caldera fiamme (CRW), and mafic enclave WSW1, which provided both good bulk sample and glass data (see text for details). Additional plots of trace element variation in glasses and bulk pumice and fiamme can be found in Fig. 2 in Supplementary Data Electronic Appendix 2. *Glass compositions are an average of multiple analyses from a given sample, and bulk-rock data for distal outflow pumice clasts have been averaged for the trace element plots (c) and (d).

(Fig. 4) shows extreme progressive enrichment in REE with increasing atomic number (from La to Lu), with a prominent positive Ce-anomaly; it should be noted that the La concentration is very low (Table 5), at sub-ppm levels, and can be readily affected by minute inclusions of LREE-bearing minerals or glass; thus, La is not considered in our analysis and is excluded from some of our zircon REE plots. The average titanite composition (Fig. 4) displays depletion in HREE relative to LREE and MREE, with much higher REE concentrations than zircon, particularly for the LREE and MREE. The subtler depletion in LREE relative to MREE reflects the very strong enrichment of the MREE in titanite relative to melt (see Colombini *et al.*, 2011), and the fact that bulk pumice and fiamme and glasses are enriched in LREE relative to the MREE. A moderate negative Eu-anomaly is apparent in both zircon and titanite patterns.

Normalized REE plots for zircon and titanite are shown in Figs 5 and 6. Zircon from high-silica rhyolites shows core-to-edge depletion in REE (Fig. 5, Table 5), particularly for the LREE and MREE. Titanite from the high-silica rhyolites shows progressive depletion in the MREE from core to edge (Fig. 6, Table 6); MREE are particularly enriched in titanite cores in high-silica rhyolite WSW2A (Fig. 6c and d).

Table 3: Bulk densities and phenocryst assemblages of outflow pumice clasts and fiamme and intra-caldera fiamme determined by thin-section analysis, X-ray tomography, and SEM analysis

Sample name	Bulk density (g cm^{-3})	Alkali feldspar	Plagioclase	Quartz	Zircon	Titanite	Allanite + chevkinite	Amphibole	Biotite	Opx	Cpx	Apatite
KPST01A	1·41	o			o	o	o	o				
KPST01B	1·41	o	o		x	o	o	o	x			
KPST01C	1·23	o	o		o	o	x	o	o			
KPST01D	1·35	o	o	s	x	o	x	x	o			
KPST01E	1·14	o	o		o	o	x	o	o			
GJ1A	–	t	t		t	t			t			
GJ1B	–	t		t	t	t			t			
GJ1C	–	t	t		t				t			
PT1B	–				t	t			t			
WSW1	–		t				t	t		t	t	
WSW2A	1·49	o	o		o	o	o	o	o			
WSW2B	1·59	o	o		o	o	o	x	o		t	
WSW2D	–	t	t	t	t	t	t	t	t			
WSW2G	–	t	t		t	t		t	t			
WSW3A	–	t	t		t	t	t	t	t		t	
WSW4B	–	t	t		t	t	t	t	t		t	
WSW4D	–	t	t		t	t	t		t			
CRW	2·53	o	o		o	x	o	x	o			o
PSTG01C	2·57	o			o	o	o	o	o			

o, thin-section analysis plus X-ray tomography and/or SEM; s, SEM only; t, thin-section analysis only; x, X-ray tomography only.

The REE patterns of zircon crystals from the low-silica rhyolites are similar to those of the high-silica rhyolites, but the REE are enriched by an order of magnitude in grain cores over edges (Fig. 5e–h). Cores and interiors of low-silica rhyolite titanite (Fig. 6e and f) are generally depleted in REE; the edges of low-silica rhyolite titanite contrast markedly with those in high-silica rhyolite, being enriched by an order of magnitude in the MREE relative to cores and interiors.

Zircon REE patterns from trachytes are similar to those of the low-silica rhyolites, but edges in one trachyte (CRW) are more variable in total REE abundance. Trachyte titanite (Fig. 6g and h) displays similar patterns to those of the low-silica rhyolite (WSW2B).

Variations in specific REE

We focus on variations in Yb, Gd, and Nd because these elements are strongly partitioned into zircon, titanite, and allanite + chevkinite, respectively. We use Hf as an indicator of fractionation in zircon (higher abundance indicates more fractionated; Claiborne *et al.*, 2006), and Gd as an indicator of fractionation in titanite (lower abundance indicates more fractionated; Colombini *et al.*, 2011). In high-silica rhyolite zircon, Hf increases from core to edge, whereas Gd (Fig. 7a and b, Table 5) and Nd decrease, with no appreciable change in Yb content (see also Supplementary Data Electronic Appendix 2 for Nd and Yb plots). Similarly, Nd, Yb, and Gd in titanite (Fig. 8a and b, Table 6; see also Supplementary Data Electronic Appendix 2) decrease from core to edge. In low-silica rhyolite zircon, Gd, Nd, and Yb all decrease from core to edge, but Hf variations are less systematic (Fig. 7c and d, Table 5; see also Supplementary Data Electronic Appendix 2). Yb, Nd, and Gd contents in one low-silica rhyolite sample (WSW2B) generally increase from core to edge, although some cores are noticeably enriched in these elements relative to edges. Titanite from the other low-silica rhyolite (GJ1A) was not analyzed because no grains were recovered in the mineral separates. Trachyte zircon edges are generally depleted in Hf, Gd and Yb relative to cores (Fig. 7e and f; see also Supplementary Data Electronic Appendix 2), whereas Yb, Nd, and Gd increase from core to edge in titanite (Fig. 8d, Table 6; see also Supplementary Data Electronic Appendix 2).

Concentrations of Ti in zircon and Zr in titanite

Variations in Ti in zircon and Zr in titanite are important because of their potential as thermobarometers. We defer

Table 4: Average glass geochemistry and zircon saturation temperatures of outflow high-silica rhyolite pumice clasts, an intra-caldera trachyte fiamma, a mafic enclave, and the primary and secondary standards analyzed

	Outflow high-silica rhyolite KPST01	Intra-caldera trachyte CRW	Mafic enclave WSW1	Primary standard NIST 610	Secondary standard NIST 612
Mg	987	$2{\cdot}54 \times 10^3$	$1{\cdot}13 \times 10^4$	465	60·4
Al	$6{\cdot}25 \times 10^4$	$7{\cdot}36 \times 10^4$	$9{\cdot}50 \times 10^4$	$1{\cdot}00 \times 10^4$	$1{\cdot}00 \times 10^4$
Si	$3{\cdot}55 \times 10^5$	$3{\cdot}51 \times 10^5$	$3{\cdot}51 \times 10^5$	$3{\cdot}28 \times 10^5$	$3{\cdot}36 \times 10^5$
P	264	372	$3{\cdot}01 \times 10^3$	343	40·6
Ca	$3{\cdot}01 \times 10^3$	$6{\cdot}59 \times 10^3$	$3{\cdot}67 \times 10^4$	$8{\cdot}18 \times 10^4$	$8{\cdot}35 \times 10^4$
Sc	3·36	6·15	17·7	441	36·1
Ti	814	$1{\cdot}68 \times 10^3$	$9{\cdot}30 \times 10^3$	434	36·6
V	1·87	14·2	86·4	442	37·1
Cr	18·6	3·63	51·1	405	36·0
Mn	464	187	473	433	36·7
Fe	$5{\cdot}03 \times 10^3$	$1{\cdot}38 \times 10^4$	$6{\cdot}18 \times 10^4$	458	55·4
Co	21·0	2·07	9·48	405	33·9
Ni	4·94	2·89	47·5	444	37·6
Cu	221	12·3	30·0	430	35·6
Zn	42·1	30·3	284	457	35·6
Ga	22·1	20·3	34·1	438	36·0
Rb	295	245	171	431	31·6
Sr	4·93	340	$1{\cdot}81 \times 10^3$	497	75·0
Y	24·4	34·6	42·2	450	36·5
Zr	152	656	529	440	36·9
Nb	39·5	15·0	28·6	419	33·8
Cs	4·83	2·77	38. 8	361	40·4
Ba	9·54	$1{\cdot}82 \times 10^3$	$2{\cdot}70 \times 10^3$	424	36·8
La	61·5	109	204	457	36·9
Ce	105	189	319	448	38·1
Pr	8·98	19·0	42·0	430	36·1
Nd	25·0	68·1	155	431	35·1
Sm	3·82	10·6	22·2	450	36·3
Eu	0·25	2·42	4·82	461	34·7
Gd	3·30	8·54	14·0	420	36·8
Tb	0·49	1·19	1·64	443	34·5
Dy	3·58	7·12	8·66	427	37·1
Ho	0·83	1·39	1·51	449	35·2
Er	2·40	3·66	4·11	426	34·8
Tm	0·42	0·50	0·50	420	38·4
Yb	3·31	3·48	3·78	461	35·2
Lu	0·51	0·50	0·59	435	34·5
Hf	7·01	14·1	13·5	418	30·2
Ta	2·00	0·77	10·9	377	35·8
Pb	45·9	47·5	38·9	414	36·3
Th	43·5	22·1	145	451	37·1
U	9·14	3·27	23·7	457	60·4
Average zircon saturation T (°C)*	778	918	832		

All values are in ppm.
*Zircon saturation temperatures calculated using the equation of Watson & Harrison (1983).

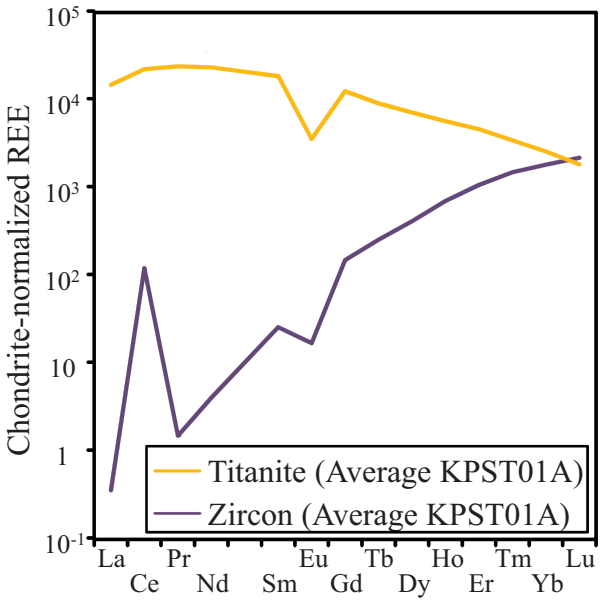

Fig. 4. Chondrite-normalized average zircon and titanite REE patterns that are used in the zircon- and titanite-normalized plots (Figs 5 and 6; see text for details). We have normalized to zircon and titanite to better resolve the differences between analyses, which are not as clear on a traditional chondrite-normalized plot. Zircon and titanite analyses from one of the most evolved pumice clasts (KPST01A) were averaged and used for this normalization. The zircon composition used for normalization shows a characteristic progressive enrichment in REE with increasing atomic number (from La to Lu), whereas titanite is enriched in MREE over both LREE and HREE. Pr concentrations were not determined for zircon; the plotted values in Figs 4 and 5 are extrapolated from Sm and Nd.

discussion of specific temperatures to a later section; suffice it to note here that higher Ti in zircon and Zr in titanite very probably correlate with higher temperatures (Ferry & Watson 2007; Hayden *et al.* 2008). Both cores and edges show a negative correlation between Ti and Hf in zircon (Fig. 9a and b, Table 5), and a positive correlation between Zr and Gd in titanite (Fig. 9c and d, Table 6); both suggest lower temperatures for the more evolved melts. Ti variations in zircon are more pronounced than Zr variations in titanite, suggesting a larger temperature interval for zircon crystallization.

In high-silica rhyolite zircon, cores have generally higher concentrations and a wider range of Ti than edges; Zr concentrations in titanite show a similar pattern, with edges that preserve the lowest Zr and Gd of the sample set. The two low-silica rhyolites show different patterns, with an increase in Ti in zircon and Zr in titanite from core to rim in WSW2B and a decrease in Ti in zircon from core to rim in GJ1A (Figs 9a, b and 10a). Cores of GJ1A zircon record the highest Ti contents of all samples, including the trachytes, suggesting the highest temperatures at the onset of zircon growth; however, the edges are similar to those in the high-silica rhyolite. Cores in trachyte zircon and titanite are similar to the high- and low-silica rhyolites; zircon edges, in contrast, record much higher Ti, up to ~50 ppm, suggesting a marked increase in temperature during edge crystallization. Titanite crystals were not found in CRW (except for small, ragged remnants identified by tomography; see below). Titanite from the other trachyte (PSTG01C) is similar to that in the low-silica rhyolite, WSW2B.

Textures

Crystal size distributions (CSDs)

Exponential CSDs, which appear 'linear' on semi-log plots, are typical of igneous rocks and can be modeled using simple nucleation and growth regimes (Marsh, 1998). As a result, description and discussion of CSD results will focus on divergence from this 'typical' shape. We characterize some of the distributions found here as 'kinked', in which two exponential segments can be recognized: a shallow-sloped tail characteristic of large crystal sizes and a steeply sloped section showing enrichment (one or more orders of magnitude) in small crystals. Power-law, or fractal, size distributions appear concave-up in semi-log plots but linear on log–log plots. Unless otherwise noted, size distributions describe crystals ~17·5–840 μm in size; sizes given are the centers of bins and not the maximum or minimum crystal size in a given bin.

Zircon. Zircon size distributions in the high-silica rhyolites, low-silica rhyolite, and trachytes are similar (Fig. 11a) and can be best described as following a simple exponential trend; the zircon size distributions of the trachytes show a kink in the 52·5 μm bin, being relatively enriched in crystals in the 26·3 μm bin.

Titanite. Titanite size distributions in the outflow high- and low-silica rhyolite (Fig. 11b) are strongly kinked, with a sharp enrichment in smaller crystals; KPST01C is more curved and KPST01E displays a linear pattern. The kink occurs in different bins for different samples (52·5 μm for KPST01D and WSW2B; 105 μm for other KPST01 samples and WSW2A). Trachyte titanite size distributions are also kinked, but differ in that they show a shallow-sloped linear portion for crystals >210 μm, and a concave-down portion for smaller crystals; crystals >210 μm are 1–2 orders of magnitude less abundant than in the rhyolites.

Allanite + chevkinite. All allanite + chevkinite size distributions are similar (Fig. 11c), with most displaying concave-up patterns that can be reasonably described by power-law (or fractal) functions. Some are more noticeably kinked than others (e.g. WSW2B, PSTG01C). We note that the allanite or chevkinite crystals are euhedral, precluding an origin by fragmentation (see Bindeman, 2005; Pamukcu & Gualda, 2010; Pamukcu *et al.*, 2012). Fragmentation is therefore not the only cause of fractal distributions; however, their origin in Peach Spring Tuff samples remains puzzling.

Magnetite. Magnetite size distributions in the high-silica rhyolites range from distinctly kinked (KPST01C, 01E, WSW2A) to concave-up (KPST01A, 01B, 01D; Fig. 11d). The low-silica rhyolite is concave-up. In contrast, the magnetite size distributions in the trachytes follow a simple linear pattern and are noticeably depleted in small crystals.

Qualitative textural observations

Textural features were studied quantitatively using a combination of thin sections, crystal separates and X-ray tomograms. In the high-silica rhyolites, all the crystals tend to be euhedral to slightly subhedral in thin section, with intact cores and no reaction rims. Zoning patterns in feldspars are generally undisturbed: contacts between zones are sharp, and zone edges do not show embayments (Fig. 12). Zircon and titanite in crystal separates are typically euhedral (Fig. 12b and c), consistent with observations in thin section and tomograms (Fig. 13a, c and e). Some crystals are fragmented, but fragmentation is not widespread.

Textures of phenocrysts in one low-silica rhyolite (WSW2B) are similar to those in the high-silica rhyolite, but phenocrysts in other low-silica rhyolite outflow pumices and fiamme are less pristine. In these samples, many feldspar phenocrysts are fragmented, and large crystals show modest embayments and rounded edges.

Trachyte fiamme, particularly CRW, display striking evidence of resorption and reaction. In PSTG01C, many feldspar phenocrysts are moderately embayed and/or have corroded cores. In CRW, nearly all the feldspars are heavily embayed, a feature that is visible in both thin sections and tomograms (Figs 12 and 13). Zircon crystals in thin sections and separates from trachytes are generally rounded (Fig. 12). Titanite could not be found in thin sections or crystal separates from CRW, but tomography provides striking images of titanite crystals that are mostly sieve-textured, with only a fraction of what we infer to be the original crystal remaining (Fig. 13). Small anhedral

Table 5: Average core, interior, and edge zircon geochemistry from outflow high-silica rhyolites, outflow low-silica rhyolites, and intra-caldera trachytes

	Outflow high-silica rhyolite KPST01A			Outflow high-silica rhyolite WSW2A			Outflow low-silica rhyolite WSW2B		
	Core	Interior	Edge	Core	Interior	Edge	Core	Interior	Edge
P	357	234	211	355	271	235	552	234	300
Sc	55·4	52·3	53·4	60·1	62·3	55·9	62·3	47·7	50·2
Ti	14·3	12·0	8·59	12·7	8·97	8·42	19·1	17·4	24·8
Fe	1·19	1·06	1·36	2·08	1·11	0·981	1·76	0·94	1·17
Y	$1·89 \times 10^3$	953	992	$1·56 \times 10^3$	985	927	$3·11 \times 10^3$	827	838
Nb	10·2	8·3	13·2	8·52	14·1	13·6	27·0	7·82	5·56
La	0·079	0·072	0·166	0·076	0·022	0·032	0·382	0·028	0·050
Ce	119	65·1	92·6	88·9	88·4	88·3	223	85·6	82·8
Nd	4·15	1·59	1·17	2·86	0·923	0·757	5·86	1·53	1·92
Sm	8·89	3·15	2·22	5·88	1·74	1·67	14·2	3·14	4·03
Eu	2·14	0·977	0·527	1·83	0·50	0·45	2·82	0·95	1·30
Gd	67·9	25·1	17·8	47·3	16·7	15·5	116	24·5	29·5
Tb	20·7	7·95	6·30	14·7	6·18	5·93	37·6	7·97	9·38
Dy	210	92·4	78·7	157	75·8	73·2	376	86·4	97·8
Ho	78·1	36·8	34·6	60·3	34·2	32·3	134	33·2	35·3
Er	313	168	172	264	175	167	526	147	150
Tm	62·5	37·1	39·9	54·9	40·7	39·1	97·8	30·2	28·9
Yb	485	310	350	436	361	340	715	252	222
Lu	83·2	56·8	65·2	78·6	68·6	64·1	113	43·8	38·2
Hf	$1·00 \times 10^4$	$1·03 \times 10^4$	$1·13 \times 10^4$	$1·04 \times 10^4$	$1·14 \times 10^4$	$1·17 \times 10^4$	$1·00 \times 10^4$	$1·04 \times 10^4$	$9·52 \times 10^4$
Th	368	182	365	297	325	347	748	192	105
U	200	148	264	189	255	266	336	127	64·8

(continued)

Table 5: Continued

	Outflow low-silica rhyolite GJ1A			Intra-caldera trachyte PSTG01C			Intra-caldera trachyte CRW			Primary standard MAD (zircon)
	Core	Interior	Edge	Core	Interior	Edge	Core	Interior	Edge	
P	$1{\cdot}33 \times 10^3$	391	429	435	232	237	345	329	266	172
Sc	85·1	58·6	29·5	47·1	58·5	61·6	50·0	72·2	61·6	10·6
Ti	34·8	16·6	14·5	19·1	28·2	34·2	19·1	29·0	29·7	25·6
Fe	0·543	0·208	0·230	1·65	1·40	1·72	3·61	1·19	1·32	4·5
Y	$7{\cdot}89 \times 10^3$	$1{\cdot}96 \times 10^3$	$1{\cdot}62 \times 10^3$	$2{\cdot}63 \times 10^3$	695	467	$1{\cdot}51 \times 10^3$	$1{\cdot}06 \times 10^3$	$1{\cdot}06 \times 10^3$	960
Nb	97·0	22·2	17·1	12·4	3·88	1·78	9·30	6·15	4·69	65
La	0·069	0·013	0·035	0·056	0·031	0·022	0·047	0·055	0·070	0·04
Ce	654	160	117	169	70·1	58·4	110	112	79·7	139
Nd	13·3	2·71	1·82	7·33	2·75	1·83	2·94	5·05	4·22	2·18
Sm	37·9	7·02	5·73	16·0	4·59	3·42	6·30	7·66	6·36	4·36
Eu	5·56	1·56	0·881	3·92	1·97	1·72	1·55	2·72	2·82	0·362
Gd	322	59·4	50·5	113	28·0	21·0	50·5	49·6	43·2	26
Tb	99·7	19·2	17·3	34·1	8·04	5·75	16·1	13·5	11·8	8·25
Dy	993	207	186	336	79·1	55·8	169	130	120	85
Ho	339	77·3	68·7	116	28·8	19·6	62·9	45·5	43·8	32
Er	$1{\cdot}22 \times 10^3$	320	266	433	117	78·5	260	178	181	153
Tm	211	63·7	48·8	77·7	23·2	15·7	51·6	33·8	36·3	36
Yb	$1{\cdot}41 \times 10^3$	490	341	553	185	125	401	256	282	325
Lu	207·1	85·6	55·2	90·1	33·3	23·3	69·5	44·9	49·7	60
Hf	$8{\cdot}40 \times 10^4$	$9{\cdot}95 \times 10^4$	$9{\cdot}58 \times 10^4$	$9{\cdot}23 \times 10^3$	$8{\cdot}69 \times 10^3$	$8{\cdot}10 \times 10^3$	$1{\cdot}00 \times 10^4$	$8{\cdot}51 \times 10^3$	$8{\cdot}84 \times 10^3$	$1{\cdot}63 \times 10^5$
Th	$2{\cdot}91 \times 10^3$	548	219	467	78·1	35·8	356	159	170	$1{\cdot}17 \times 10^3$
U	829	282	135	180	52·2	18·2	234	70	95	$4{\cdot}20 \times 10^3$

All values are in ppm.

crystals of titanite can also be found in tomograms of the trachytes. Similarly, small anhedral crystals of amphibole are found in tomograms of the trachyte samples, although small euhedral crystals can also be found.

An additional intriguing textural feature in the Peach Spring Tuff is a strong tendency for accessory minerals to cluster together. In the outflow samples it is most common to find zircon and allanite + chevkinite crystals attached to or included within magnetite and titanite crystals. It is also relatively common, particularly in the more distal outflow high-silica rhyolite samples, to find accessory minerals included in or attached to amphibole crystals. This texture is evident in thin sections of these samples, but it is most strikingly illustrated in 3D renditions of the accessory minerals derived from tomography. For example, Fig. 14 shows the suite of accessory minerals rendered from an outflow high-silica rhyolite pumice clast (KPST01C). It should be noted that when the titanite and magnetite crystals are hidden, it becomes clear that most of the zircon in the sample is concentrated in clusters in and around the titanite and magnetite crystals (see Gualda *et al.*, 2010). Clustering of accessory minerals also occurs in intra-caldera fiamme, but it is less common than in the outflow samples. In thin sections of intra-caldera fiamme, magnetite, zircon, and allanite + chevkinite cluster together. In tomograms of these samples, titanite is also found associated with allanite + chevkinite, zircon, and/or magnetite. It should be emphasized that not all crystals of accessory minerals are found in clusters.

Rhyolite-MELTS results

High-silica rhyolite simulations

Simulations with the high-silica end-member composition (KPST01D) reveal nearly invariant behavior upon saturation in two feldspars, quartz and water (Fig. 15a and c); the nearly invariant temperature (742°C) is the same for all total water contents investigated (2, 3, 5 and 7 wt % H_2O), which is expected considering that a single pressure was used—leading to the same final assemblage in all cases (see Gualda *et al.*, 2012*a*). Liquidus temperatures decrease with increasing total water (e.g. 886°C for 2 wt % H_2O, 781°C for 7 wt % H_2O), directly controlling the temperature range over which crystallization takes place (hereafter crystallization interval).

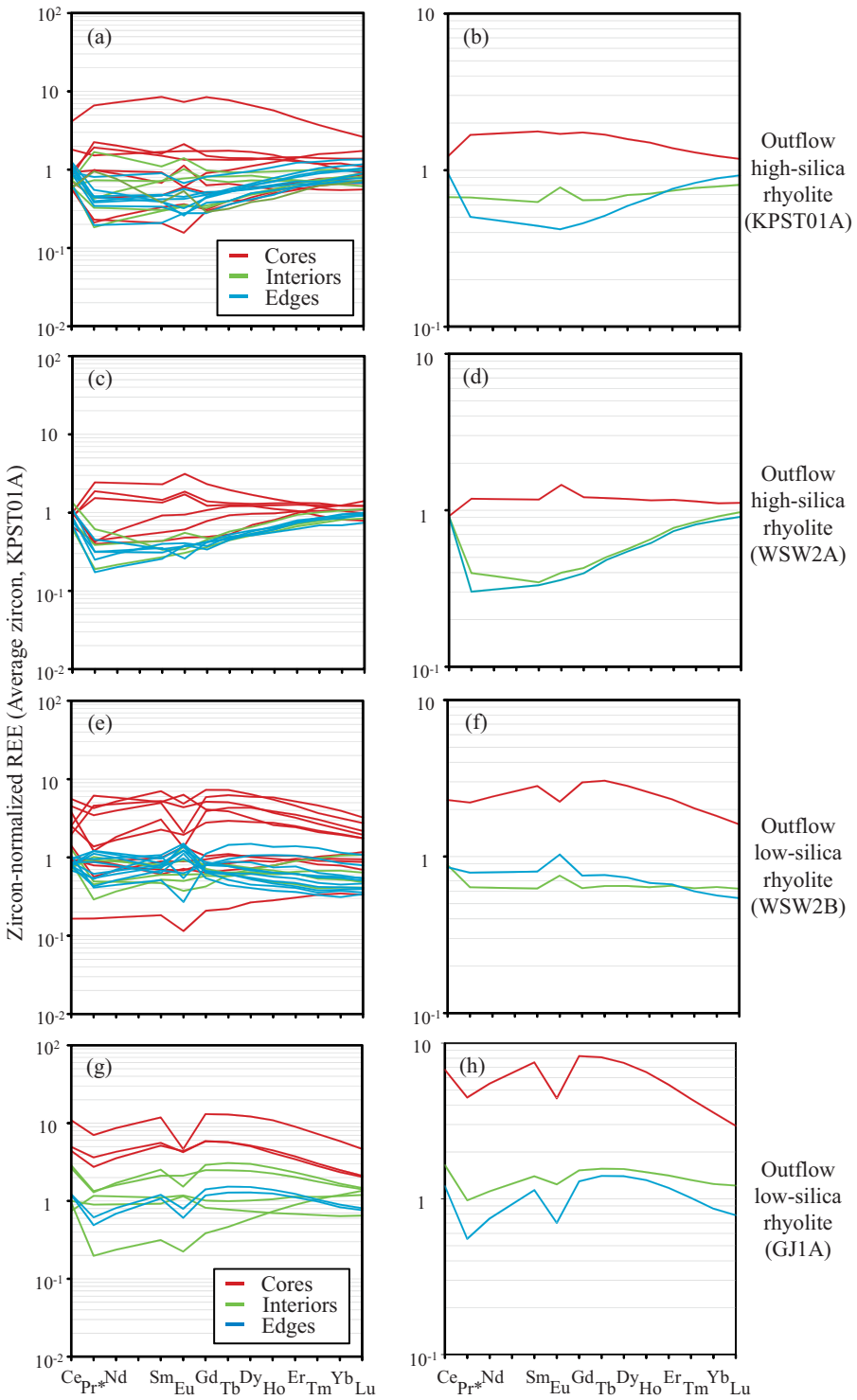

Fig. 5. Zircon-normalized REE patterns for zircon from (a–d) the outflow high-silica rhyolites, (e–h) the outflow low-silica rhyolites, and (i–l) the intra-caldera trachytes. All analyses for a given sample are plotted in the left-hand column, and average core, edge, and interior analyses are shown in the right-hand column. Starred elements were not measured; their data points are projections through adjacent elements. The REE values for the average zircon (KPST01A) used for normalization (see text for details) are (in ppm): Ce 97·0; Nd 2·40; Sm 5·03; Eu 1·30; Gd 39·0; Tb 12·3; Dy 133; Ho 52·1; Er 226; Tm 48·1; Yb 394; Lu 70·4.

(continued)

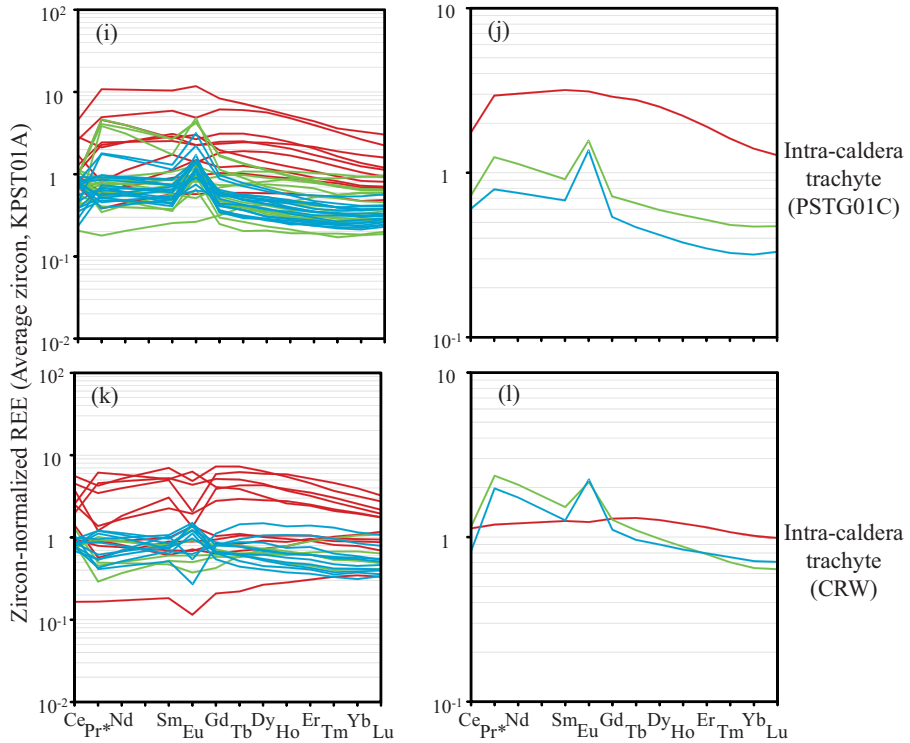

Fig. 5. Continued.

Unfortunately, the saturation sequence predicted by rhyolite-MELTS (sanidine → quartz → plagioclase) is inconsistent with our petrographic observations in that plagioclase phenocrysts are ubiquitous and much more abundant than quartz phenocrysts (see Gualda *et al.*, 2012*a*). Fortunately, our aim in using the rhyolite-MELTS simulations is not to model in detail the crystallization of the Peach Spring Tuff, but rather to retrieve critical information on several quantities of interest; namely, estimates of the crystallization interval, temperature versus enthalpy curves, and titania and silica activities. Considering that heats of crystallization of quartz and plagioclase in rhyolitic melts are very similar to each other (M. Ghiorso, personal communication), the effect of the incorrect sequence of saturation on these quantities is minor to negligible. As such, we consider that rhyolite-MELTS provides us with adequate estimates of the parameters of interest. It is noteworthy that other means of estimating these quantities from thermodynamic data are likely to be less accurate (Ghiorso & Gualda, 2013).

Trachyte simulations

Simulations with the CRW trachyte composition were run over a wider range of total H_2O (0·25, 0·5, 1, 2, 3, 5 and 7 wt %; Fig. 15b and d). Similarly to the high-silica rhyolites, the crystallization interval for the trachytes is variable, and is a strong function of the variation in liquidus temperature as a function of H_2O content (e.g. 807°C for 7 wt % H_2O, 1057°C for 0·25 wt % H_2O). In all simulations, sanidine is the highest-temperature felsic phase to crystallize, with quartz as the lowest-temperature felsic phase; this is consistent with the absence of quartz and coexistence of sanidine and plagioclase in the trachytes, showing good agreement between rhyolite-MELTS predictions and petrography.

Titania and silica activities and Ti-in-zircon and Zr-in-titanite temperatures

Rhyolite-MELTS simulations indicate that over the 700–1100°C temperature range investigated, a_{TiO2} and a_{SiO2} vary significantly for both the high-silica rhyolite and the trachyte (Fig. 16). Titania activity for the various runs ranges from ~0·1 to 0·5 for the high-silica rhyolite, and from ~0·2 to 0·5 for the trachyte (Fig. 16a). Silica activity variations are in the range of 0·8–1 in the high-silica rhyolite and 0·65–1 in the trachyte (Fig. 16b). These values represent calculated activities for the entire crystallization interval, from near-solidus to near-liquidus, with the lowest values indicated being above liquidus for runs with high water concentration. Titania and silica activities are positively correlated, such that lower a_{TiO2} is associated with lower a_{SiO2}, and both a_{TiO2} and a_{SiO2} decrease with increasing temperature. Recently, the results of Huang & Audetat (2012) suggest that MELTS, and consequently rhyolite-MELTS, gives more realistic

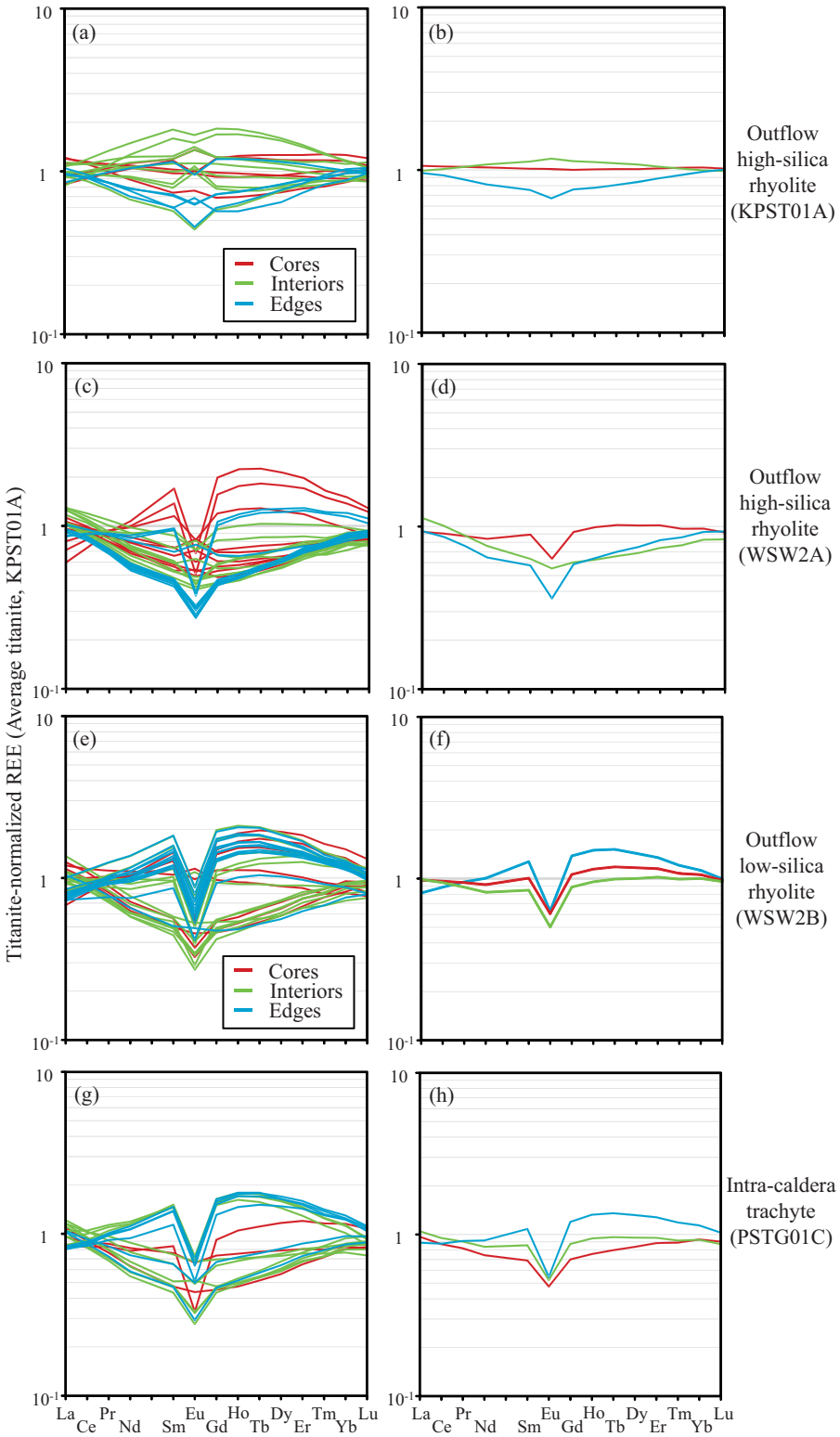

Fig. 6. Titanite-normalized REE patterns for titanite from (a–d) the outflow high-silica rhyolites, (e, f) an outflow low-silica rhyolite (WSW2B), and (g, h) an intra-caldera trachyte (PSTG01C). Titanite was not found in the other trachyte sample (CRW). All analyses for a given sample are plotted in the left-hand column, and average core, edge, and interior analyses are shown in the right-hand column. The REE values for the average titanite (KPST01A) used for normalization (see text for details) are (in ppm): La 4410; Ce 17 930; Pr 3020; Nd 15 870; Sm 4320; Eu 360; Gd 3990; Tb 530; Dy 2720; Ho 490; Er 1110; Tm 130; Yb 620; Lu 67·4.

estimates of a_{TiO2} than does the solubility model of Hayden & Watson (2007) or Fe–Ti oxides (see also Ghiorso & Gualda, 2013).

Ti-in-zircon and Zr-in-titanite temperature calculations both include a_{TiO2} and a_{SiO2}. Because rhyolite-MELTS simulations yield both a_{TiO2} and a_{SiO2} for any given temperature, it is possible to calculate the equilibrium concentrations of Ti in zircon and Zr in titanite as a function of temperature (assuming $a_{ZrSiO4}=1$ and $P=250$ MPa). Effectively, the Ti-in-zircon and Zr-in-titanite temperatures can be calculated by finding the appropriate temperature that yields the right combination of activities and Ti or Zr concentrations. In practice, we linearly interpolate the activities between each point calculated using rhyolite-MELTS (determined at 50°C steps; Fig. 16a and b) to yield a_{TiO2}, a_{SiO2}, Ti in zircon, and Zr in titanite as a function of temperature (in 5°C steps; see Fig. 16c and d); for each zircon or titanite analysis, we find the closest match in Zr and Ti, and use the corresponding a_{TiO2} and a_{SiO2} to calculate the best estimate of temperature.

Several features of the temperature versus concentration (Ti in zircon and Zr in titanite) curves stand out. For

Table 6: Average core, interior, and edge titanite geochemistry from outflow high-silica rhyolites, an outflow low-silica rhyolite, and an intra-caldera trachyte

	Outflow high-silica rhyolite KPST01A			Outflow high-silica rhyolite WSW2A		
	Core	Interior	Edge	Core	Interior	Edge
Mg	902	902	861	900	836	865
P	285	280	206	249	288	200
Al	9161	9617	9565	9456	8844	9081
Ti	$2{\cdot}22\times10^5$	$2{\cdot}19\times10^5$	$2{\cdot}17\times10^5$	$2{\cdot}16\times10^5$	$2{\cdot}17\times10^5$	$2{\cdot}14\times10^5$
V	243	207	152	168	170	128
Cr	4·11	2·95	1·29	1·69	1·61	4·43
Mn	$2{\cdot}11\times10^3$	$2{\cdot}33\times10^3$	$2{\cdot}75\times10^3$	$2{\cdot}53\times10^3$	$2{\cdot}46\times10^3$	$3{\cdot}07\times10^3$
Fe	$2{\cdot}21\times10^4$	$2{\cdot}27\times10^4$	$2{\cdot}29\times10^4$	$2{\cdot}31\times10^4$	$2{\cdot}12\times10^4$	$2{\cdot}24\times10^4$
Sr	49·0	48·4	47·6	47·0	47·3	46·4
Y	$9{\cdot}19\times10^3$	$9{\cdot}57\times10^3$	$8{\cdot}24\times10^3$	$1{\cdot}05\times10^4$	$7{\cdot}64\times10^3$	$8{\cdot}53\times10^3$
Zr	$1{\cdot}44\times10^3$	$1{\cdot}53\times10^3$	$1{\cdot}15\times10^3$	$1{\cdot}48\times10^3$	$1{\cdot}25\times10^3$	978
Nb	$2{\cdot}41\times10^3$	$2{\cdot}06\times10^3$	$2{\cdot}24\times10^3$	$2{\cdot}18\times10^3$	$2{\cdot}67\times10^3$	$2{\cdot}70\times10^3$
Ba	9·93	10·1	8·95	7·74	10·1	7·42
La	$4{\cdot}89\times10^3$	$4{\cdot}56\times10^3$	$4{\cdot}41\times10^3$	$4{\cdot}10\times10^3$	$4{\cdot}98\times10^3$	$4{\cdot}14\times10^3$
Ce	$1{\cdot}88\times10^4$	$1{\cdot}81\times10^4$	$1{\cdot}65\times10^4$	$1{\cdot}62\times10^4$	$1{\cdot}81\times10^4$	$1{\cdot}55\times10^4$
Pr	$2{\cdot}96\times10^3$	$2{\cdot}97\times10^3$	$2{\cdot}47\times10^3$	$2{\cdot}64\times10^3$	$2{\cdot}66\times10^3$	$2{\cdot}29\times10^3$
Nd	$1{\cdot}45\times10^4$	$1{\cdot}52\times10^4$	$1{\cdot}14\times10^4$	$1{\cdot}33\times10^4$	$1{\cdot}21\times10^4$	$1{\cdot}02\times10^4$
Sm	$3{\cdot}69\times10^3$	$4{\cdot}08\times10^3$	$2{\cdot}73\times10^3$	$3{\cdot}86\times10^3$	$2{\cdot}73\times10^3$	$2{\cdot}49\times10^3$
Eu	269	312	178	228	198	130
Gd	$3{\cdot}26\times10^3$	$3{\cdot}69\times10^3$	$2{\cdot}47\times10^3$	$3{\cdot}69\times10^3$	$2{\cdot}40\times10^3$	$2{\cdot}34\times10^3$
Tb	441	489	340	522	329	337
Dy	$2{\cdot}374\times10^3$	$2{\cdot}54\times10^3$	$1{\cdot}87\times10^3$	$2{\cdot}78\times10^3$	$1{\cdot}79\times10^3$	$1{\cdot}90\times10^3$
Ho	425	454	355	499	338	368
Er	997	$1{\cdot}02\times10^3$	868	$1{\cdot}13\times10^3$	820	916
Tm	114	113	103	123	97·6	109
Yb	575	553	541	598	511	571
Lu	60·6	58·5	59·7	62·0	56·3	62·9
Hf	71·2	70·4	58·8	69·8	66·3	57·2
Ta	209	168	146	166	213	177
Pb	0·373	0·409	0·427	0·382	0·376	0·390
Th	485	382	364	333	441	362
U	29·5	25·4	26·8	24·4	27·7	27·2

(continued)

Table 6: Continued

	Outflow low-silica rhyolite WSW2B			Intra-caldera trachyte PSTG			Primary standard BLR (titanite)
	Core	Interior	Edge	Core	Interior	Edge	
Mg	937	908	870	844	800	838	650
P	295	227	251	229	270	289	65·0
Al	$9{\cdot}48 \times 10^3$	$9{\cdot}57 \times 10^3$	$9{\cdot}80 \times 10^3$	$9{\cdot}44 \times 10^3$	$9{\cdot}02 \times 10^3$	$9{\cdot}60 \times 10^3$	$1{\cdot}63 \times 10^4$
Ti	$2{\cdot}18 \times 10^5$	$2{\cdot}17 \times 10^5$	$2{\cdot}16 \times 10^5$	$2{\cdot}21 \times 10^5$	$2{\cdot}25 \times 10^5$	$2{\cdot}27 \times 10^5$	$1{\cdot}98 \times 10^5$
V	144	136	128	136	134	121	100
Cr	1·17	1·12	0·653	0·844	0·625	0·750	105
Mn	$2{\cdot}90 \times 10^3$	$2{\cdot}99 \times 10^3$	$2{\cdot}82 \times 10^3$	$2{\cdot}90 \times 10^3$	$2{\cdot}88 \times 10^3$	$3{\cdot}14 \times 10^3$	$1{\cdot}00 \times 10^3$
Fe	$2{\cdot}39 \times 10^4$	$2{\cdot}35 \times 10^4$	$2{\cdot}46 \times 10^4$	$2{\cdot}41 \times 10^4$	$2{\cdot}27 \times 10^4$	$2{\cdot}52 \times 10^4$	$1{\cdot}91 \times 10^4$
Sr	47·4	47·4	46·9	5·18	4·35	3·34	50·0
Y	$1{\cdot}19 \times 10^4$	$1{\cdot}06 \times 10^4$	$1{\cdot}42 \times 10^4$	$8{\cdot}91 \times 10^3$	$9{\cdot}63 \times 10^3$	$1{\cdot}25 \times 10^4$	$3{\cdot}36 \times 10^3$
Zr	$1{\cdot}37 \times 10^3$	$1{\cdot}15 \times 10^3$	$1{\cdot}30 \times 10^3$	$1{\cdot}25 \times 10^3$	$1{\cdot}23 \times 10^3$	$1{\cdot}28 \times 10^3$	$1{\cdot}33 \times 10^3$
Nb	$2{\cdot}56 \times 10^3$	$2{\cdot}63 \times 10^3$	$2{\cdot}02 \times 10^3$	$2{\cdot}41 \times 10^3$	$2{\cdot}79 \times 10^3$	$2{\cdot}32 \times 10^3$	$3{\cdot}65 \times 10^3$
Ba	10·1	8·84	9·99	9·95	11·5	15·1	14·0
La	$4{\cdot}31 \times 10^3$	$4{\cdot}36 \times 10^3$	$3{\cdot}59 \times 10^3$	$4{\cdot}27 \times 10^3$	$4{\cdot}62 \times 10^3$	$3{\cdot}92 \times 10^3$	375
Ce	$1{\cdot}73 \times 10^4$	$1{\cdot}69 \times 10^4$	$1{\cdot}59 \times 10^4$	$1{\cdot}56 \times 10^4$	$1{\cdot}71 \times 10^4$	$1{\cdot}57 \times 10^4$	$1{\cdot}66 \times 10^3$
Pr	$2{\cdot}86 \times 10^3$	$2{\cdot}68 \times 10^3$	$2{\cdot}88 \times 10^3$	$2{\cdot}48 \times 10^3$	$2{\cdot}73 \times 10^3$	$2{\cdot}76 \times 10^3$	285
Nd	$1{\cdot}46 \times 10^4$	$1{\cdot}31 \times 10^4$	$1{\cdot}59 \times 10^4$	$1{\cdot}18 \times 10^4$	$1{\cdot}33 \times 10^4$	$1{\cdot}46 \times 10^4$	$1{\cdot}51 \times 10^3$
Sm	$4{\cdot}35 \times 10^3$	$3{\cdot}67 \times 10^3$	$5{\cdot}50 \times 10^3$	$2{\cdot}98 \times 10^3$	$3{\cdot}71 \times 10^3$	$4{\cdot}68 \times 10^3$	503
Eu	218	180	226	171	187	196	74·2
Gd	$4{\cdot}23 \times 10^3$	$3{\cdot}53 \times 10^3$	$5{\cdot}51 \times 10^3$	$2{\cdot}79 \times 10^3$	$3{\cdot}49 \times 10^3$	$4{\cdot}77 \times 10^3$	655
Tb	602	502	788	398	498	697	122
Dy	$3{\cdot}21 \times 10^3$	$2{\cdot}70 \times 10^3$	$4{\cdot}12 \times 10^3$	$2{\cdot}17 \times 10^3$	$2{\cdot}62 \times 10^3$	$3{\cdot}68 \times 10^3$	820
Ho	573	493	704	412	470	648	187
Er	$1{\cdot}28 \times 10^3$	$1{\cdot}13 \times 10^3$	$1{\cdot}50 \times 10^3$	981	$1{\cdot}06 \times 10^3$	$1{\cdot}42 \times 10^3$	525
Tm	137	126	153	113	117	151	71·5
Yb	651	616	693	574	571	700	350
Lu	65·8	64·6	67·2	60·9	58·8	69·2	35·0
Hf	68·0	58·4	59·1	65·8	67·6	68·7	52·5
Ta	213	199	160	176	239	178	225
Pb	0·391	0·417	0·351	0·359	0·345	0·337	19·7
Th	371	361	250	305	331	261	186
U	21·6	24·3	16·8	22·7	21·5	18·9	300

All values are in ppm

zircon (Fig. 16c): (1) the two different compositions (high-silica rhyolite and trachyte) yield significantly different curves; (2) the effect of water content is relatively small compared with the contrast owing to bulk composition differences. The curve for the high-silica rhyolites is so flat that Ti contents in excess of 10 ppm would require >1100°C, much above the calculated liquidus and zircon saturation temperatures; importantly, a 1 ppm difference (an order of 10% relative) in measured Ti or a difference of 0·05 in the calculated titania activity (for $a_{TiO2} = 0{\cdot}4$–$0{\cdot}5$; order of 10% relative) would lead to temperature differences of the order of 50°C. This uncertainty is very large in comparison with the uncertainty that results from independent treatment of errors in Ti or a_{TiO2} (order of ±10°C for the example above); the amplification of the uncertainty derives from the correlation between a_{TiO2}, Ti in zircon and T. Owing to the need for high precision and accuracy in both Ti measurements and activity, absolute temperatures should be interpreted with caution; but temperature differences—which require only good reproducibility—are probably very robust. It is hard to imagine that high-silica rhyolite magmas attained temperatures in excess of the liquidus (~850°C), and zircon crystallization should be restricted to temperatures

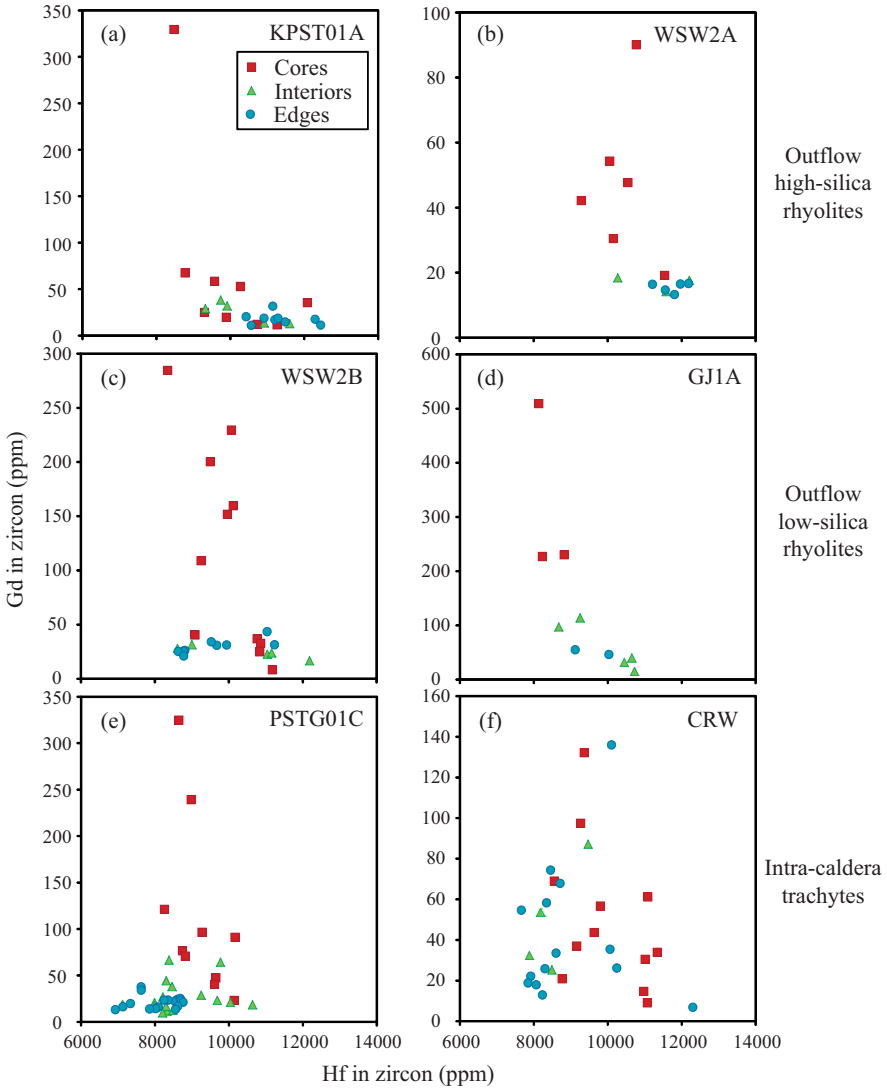

Fig. 7. Gd vs Hf in zircon from (a, b) high-silica rhyolites, (c, d) low-silica rhyolites, and (e, f) trachytes.

below the bulk pumice zircon saturation temperature (<830°C), which leads to expected Ti concentrations of 5–7 ppm. Given the accuracy challenges referred to above, we consider edge analyses (7–11 ppm Ti) to compare favorably with this range. In contrast, many core and interior analyses have Ti > 12 ppm, which we interpret to signify that they did not crystallize from a high-silica rhyolite melt; temperature estimates using these compositions are difficult to make, as they require an arbitrary choice of titania and silica activities. The case for the trachyte is not as extreme, and a concentration span from 5 to 30–40 ppm is expected for temperatures in the range 750–1100°C; nevertheless, owing to the correlation between equilibrium Ti concentration, titania and silica activities, and temperature, small biases in either Ti measurements or titania activity will lead to significant biases in absolute temperature. Because of these limitations, we focus on Ti-in-zircon temperature differences and trends, rather than on absolute values. For titanite (Fig. 16d), the Zr versus temperature relationship is highly non-linear, and is particularly shallow for temperatures <800°C. Fortunately, the Zr concentrations in titanite (i.e. >700 ppm) are two orders of magnitude higher than Ti in zircon, such that precision and accuracy in the measurements are much superior; accuracy in the activities is also less critical, as shown by the greater similarity between all the curves (Fig. 16d). As an example, for titanite with 1000 ppm, a change in composition of 100 ppm (10% relative) or a change of 0·05 in a_{TiO2} (10% relative) leads to only a 5°C temperature difference; we thus expect Zr-in-titanite temperatures to be substantially more accurate than Ti-in-zircon temperatures.

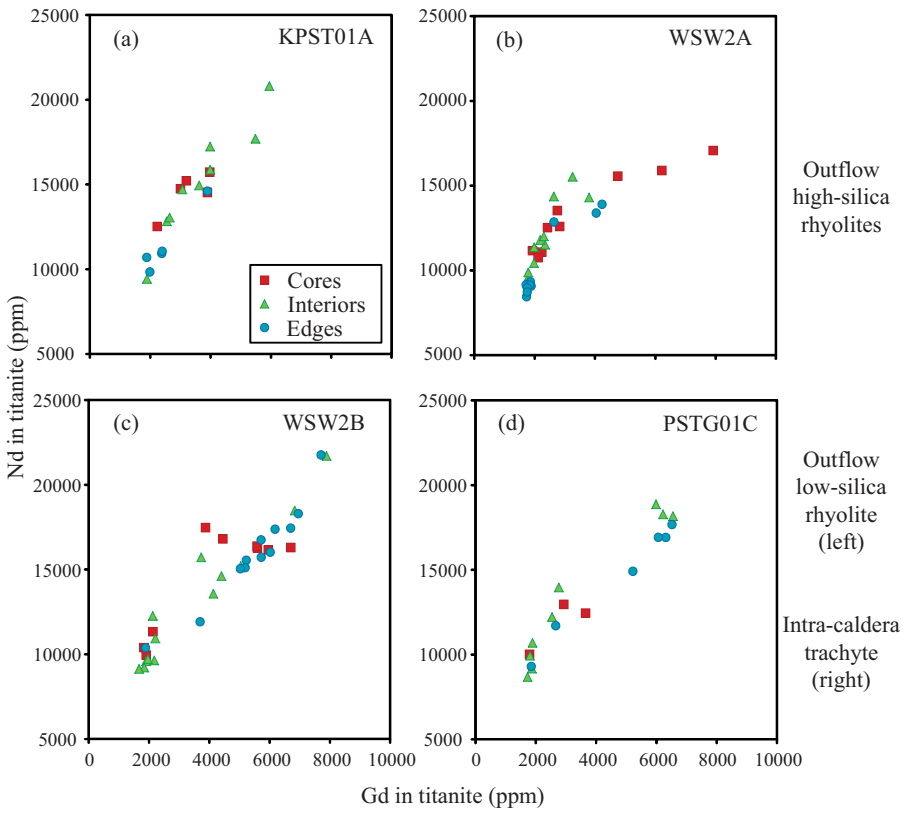

Fig. 8. Nd vs Gd in titanite from (a, b) high-silica rhyolites, (c) low-silica rhyolite, and (d) trachyte.

If we assume that a reasonable range of activity–temperature–composition relationships is encompassed by the simulations with the two extreme compositions used here, we conclude that the Ti contents necessary to achieve Ti-in-zircon temperatures of 750 and 1000°C are ~5 ppm and ~8 ppm (high-silica rhyolite) and ~34 ppm (trachyte), respectively. Similarly, the Zr contents needed to obtain Zr-in-titanite temperatures of 725°C, 750°C, and 775°C are ~770–790 ppm, 1180–1260 ppm, and ~1880–2220 ppm, respectively. These temperature ranges are plotted as reference regions in Figs 9 and 10. As mentioned above (see Methods), the effect of uncertainty in pressure on Zr-in-titanite temperatures is much smaller than the effect of uncertainties on activities and can be effectively neglected.

The calculated Ti-in-zircon temperatures are in the range 820–1220°C for high-silica rhyolites, 870–1340°C for low-silica rhyolites, and 810–1190°C for trachytes. The upper ends of these ranges, well above both liquidi and zircon saturation temperatures for the bulk pumice compositions, are clearly unrealistic and demonstrate lack of equilibrium of zircon with the coexisting glass. Thus, zircon did not grow from the host melt, so neither a_{TiO2} nor temperature can be accurately estimated. We emphasize our focus on temperature differences and trends. It is important to note that temperatures for the low-silica rhyolites were calculated with activities from high-silica rhyolite simulations, and are likely to be systematically too high (i.e. the Ti versus T curve is likely to be intermediate between that for high-silica rhyolite and trachyte). Importantly, because the Ti in zircon versus temperature curves are monotonic (see Fig. 16c and d) the zoning in Ti can be readily interpreted as reflecting temperature variations. Zircon rims in the trachytes give a temperature mode >1100°C; it seems conservative to estimate that these rims crystallized at temperatures of at least 900–1000°C.

The calculated Zr-in-titanite temperatures are much more uniform; all the data fall in the range 720–770°C, with a distinct mode at 755°C. It is striking that the rhyolite-MELTS simulations all reveal nearly invariant behavior at ~750°C and, given the Zr-in-titanite temperatures, this suggests that titanite saturated near the solidus.

DISCUSSION

The data presented above suggest an intriguing story of the pre- and syn-eruptive evolution of the Peach Spring magmatic system. They suggest the following: (1) the magmatic plumbing system ('magma body') that fed the eruption was zoned in composition, texture, and temperature;

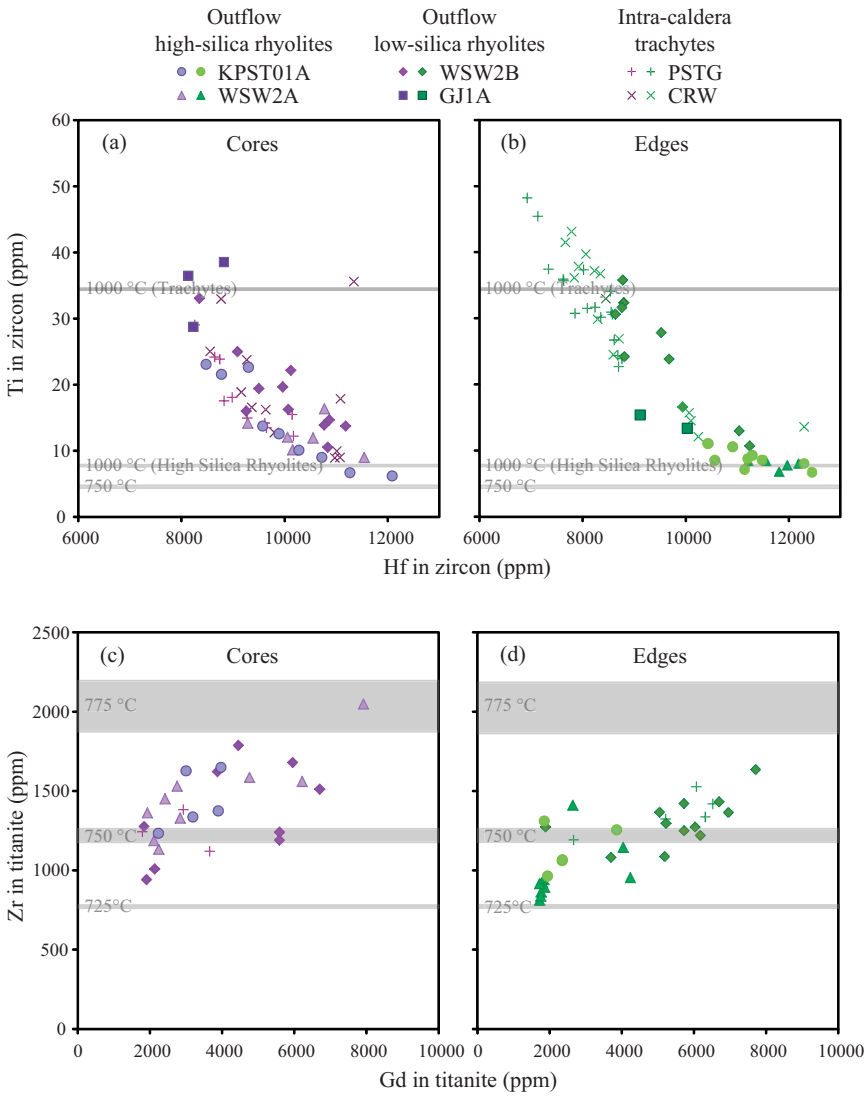

Fig. 9. Measured Ti concentrations in zircon (a, b) and Zr concentrations in titanite (c, d) for high-silica rhyolites (KPST01A, WSW2A), low-silica rhyolites (WSW2B, GJ1A), and trachytes (PSTG01C, CRW); core analyses are shown in the left-hand diagrams (a, c) and edge analyses are shown in the right-hand diagrams (b, d). Increasing concentrations of Ti in zircon and Zr in titanite are associated with increasing temperature (Ferry & Watson, 2007; Hayden *et al.*, 2008). Although uncertainties in activity determination and element concentrations make it difficult to assess absolute temperatures, we demonstrate that core-to-edge trends are direct responses to temperature fluctuations. We also display ranges in Ti and Zr content that give temperatures of 750 and 1000°C for zircon and 725°C, 750°C, and 775°C for titanite, based on ranges of titania and silica activities and pressures estimated from rhyolite-MELTS simulations ($a\mathrm{TiO_2} = 0{\cdot}1$–$0{\cdot}5$, $a\mathrm{SiO_2} = 0{\cdot}65$–$1$, $P = 250$ MPa; see text for details).

(2) shallower portions of the system had a relatively simple cooling history prior to eruption, in contrast to deeper portions that experienced a major late-stage heating event; (3) a decompression event probably occurred very near the time of eruption. We expand on these inferences below.

Zoning of the Peach Spring system

Spatial variation in the Peach Spring Tuff deposits

Our data identify a sharp distinction between intra-caldera and typical distal pumice and fiamme of the Peach Spring Tuff. Intra-caldera fiamme are crystal-rich trachyte with relatively low silica and high concentrations (in both whole-fiamme and glass) of elements compatible in the phenocryst assemblage, whereas the distal outflow pumice is a phenocryst-poor, high-silica rhyolite depleted in phenocryst-compatible elements. A thin basal layer that underlies the ignimbrite has been interpreted as either a surge (Valentine *et al.*, 1989, 1990) or a fall deposit (Wilson & Self, 1990), but in both cases as the initial phase of the Peach Spring eruption; its pumice is a uniformly

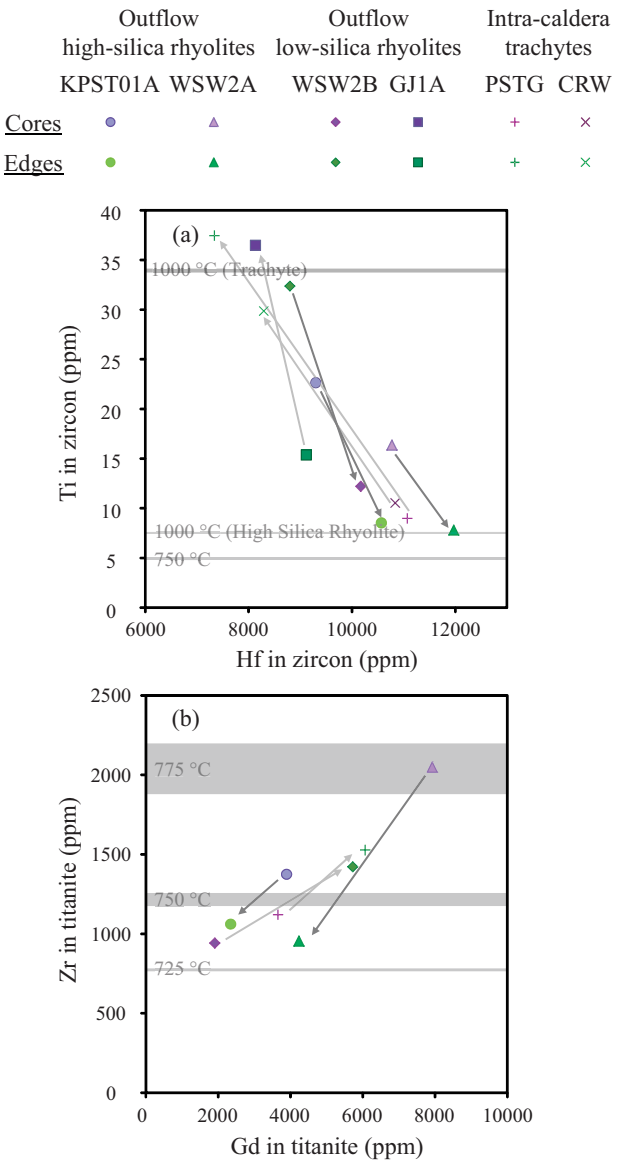

Fig. 10. Core-to-edge trends in Ti in zircon and Zr in titanite for single grains in (a) zircon and (b) titanite. Arrows connect core and edge of the same crystals. Reference temperatures are the same as in Fig. 9.

crystal-poor, high-silica rhyolite (McCracken *et al.*, 2011), much like pumice from the distal ignimbrite. Proximal outflow contains more diverse pumice and fiamme that range from dominant high-silica rhyolite, similar to that observed in the distal outflow, to low-silica rhyolite with intermediate characteristics to rare trachyte. The intra-caldera tuff was presumably the last to be erupted—after caldera collapse—indicating a transition with time from eruption of crystal-poor rhyolite to crystal-rich trachyte. We suspect that the proximal outflow deposits include the last erupted products prior to collapse.

Implications for zoning in the Peach Spring magma body

Sequences of deposits of large eruptions have commonly been interpreted to reflect the depth of origin of the magmas within the system that was tapped; that is, the shallowest material erupts first and the deepest erupts last. The feeding system is commonly envisioned as a continuous magma body or chamber (e.g. Lipman *et al.*, 1966; Smith & Bailey, 1966; Smith, 1979; Hildreth, 1981, 2004; Bacon & Druitt, 1988; Druitt & Bacon, 1989), or possibly as discrete, stacked magma bodies (Bindeman & Valley, 2003). Alternative interpretations for zoned eruption deposits invoke sequential tapping of distinct, laterally discrete magma bodies during a continuing eruption (e.g. Cooper *et al.*, 2012) and complications of the eruptive stratigraphy as a consequence of syn-eruption replenishment (see Knesel & Duffield, 2007).

Although we cannot rule out more complicated scenarios, the distinction between early, low-density, highly silicic, crystal-poor rhyolite and late, higher density, crystal-rich trachyte is consistent with a simple inversion of the magma chamber stratigraphy. Furthermore, the consistency of the phenocryst assemblage and the continuous range of bulk pumice and fiamme composition from trachyte to high-silica rhyolite—particularly when proximal samples are included—support the notion of relatively simple zonation of the magma body. Finally, textural characteristics and accessory mineral compositions imply thermal histories that may reflect processes that correlate with depth (see below).

Origin of compositional zoning in the Peach Spring magma body

As suggested above, the relatively simple and continuous variation in magma composition and phenocryst content indicated by pumice and fiamme are most simply explained by tapping of a continuous magma body. If this is correct, continuous variation presumably reflects either mixing of contrasting magmas or crystal–melt fractionation processes. With our existing dataset, we cannot rule out the possibility of involvement of open-system processes in generating the Peach Spring magmas. In fact, given its scale, it seems that this giant system must have been constructed by many repeated replenishments; however, the general pattern of variability of the erupted magmas, as represented by pumice and fiamme, is difficult to explain by mixing of unrelated magmas. First, the trachyte would have been an unusual magma and an unlikely candidate for a mixing end-member introduced into the Peach Spring magma body: (1) its high phenocryst content, presumably even higher prior to the resorption reflected in its textures, would have limited its mobility; (2) its composition—intermediate in terms of silica concentration (66–69 wt % SiO_2), but characterized by a phenocryst assemblage typical of evolved rhyolite, and very high

concentrations of elements compatible in these phenocrysts (e.g. K_2O ~6 wt %, Zr ~600 ppm, LREE ~500× chondrite)—differs from those of typical erupted magmas, both regionally and globally (e.g. Metcalf, 2004; Pearthree *et al.*, 2009). The trachyte is even more difficult to explain as a mixture, because this would require an even more extreme end-member. Although the single trachyandesite enclave (WSW1) documents some involvement of a more mafic magma in the Peach Spring system, it did not participate in any mixing process that could explain the compositions of the analyzed pumice and fiamme, as it falls far from a plausible linear trend consistent with mixing. Compositions and zoning patterns of accessory minerals are also inconsistent with mixing, which would be expected to yield crystals with differing cores but similar rim compositions. Just the opposite is true in general: zircon and titanite from trachytic and rhyolitic pumice generally have similar cores but distinctly different rims.

The simplest process by which to explain compositional variability in pumice and fiamme and apparent zonation (vertical stratification) in the Peach Spring system is by crystal–melt segregation (fractional crystallization in a

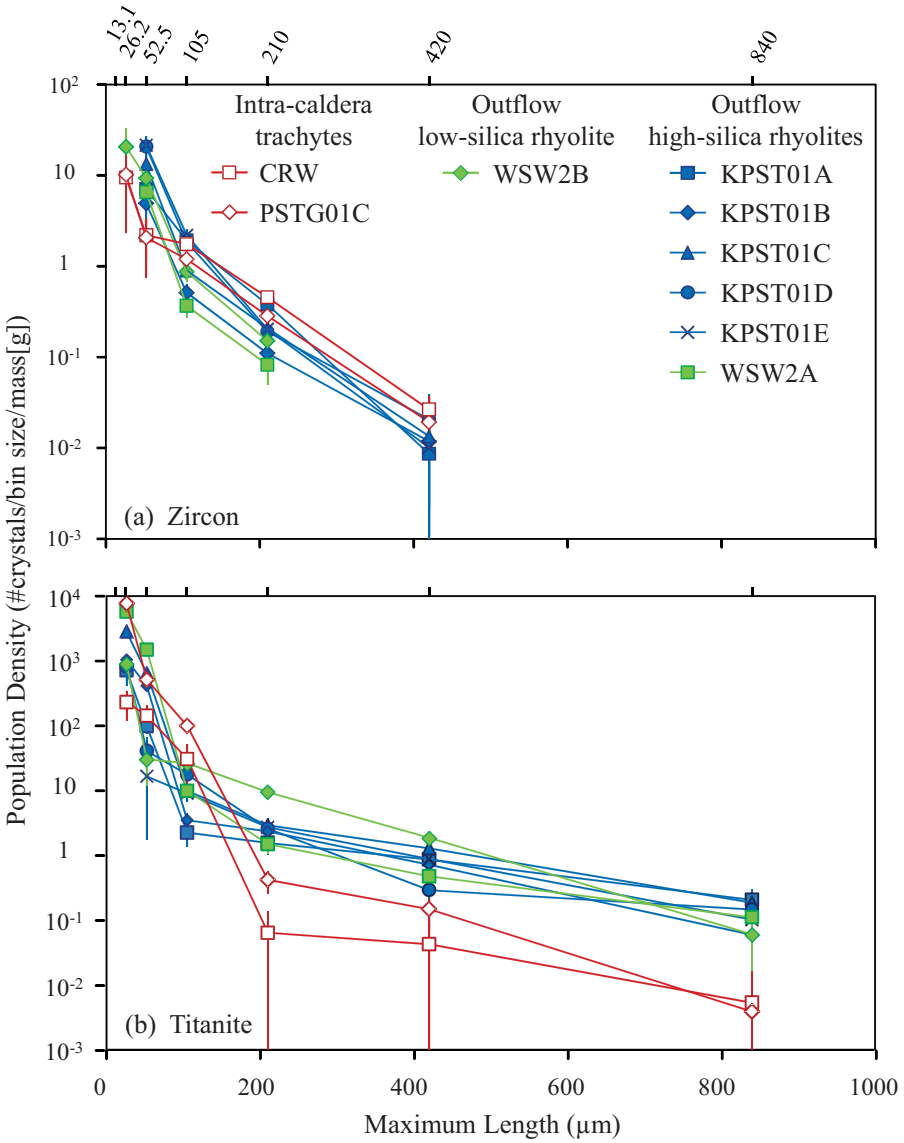

Fig. 11. Crystal size distributions obtained using X-ray tomography for (a) zircon, (b) titanite, (c) allanite + chevkinite, and (d) magnetite in Kingman (filled dark gray symbols; blue in online version of figure), Warm Springs West (filled light gray symbols; green online), and intra-caldera (open black symbols; red online) pumice and fiamme. Crystal size distributions from igneous rocks with simple nucleation and growth crystallization histories plot as straight lines on semi-log plots of crystal size (maximum length) vs population density (see text for details).

(continued)

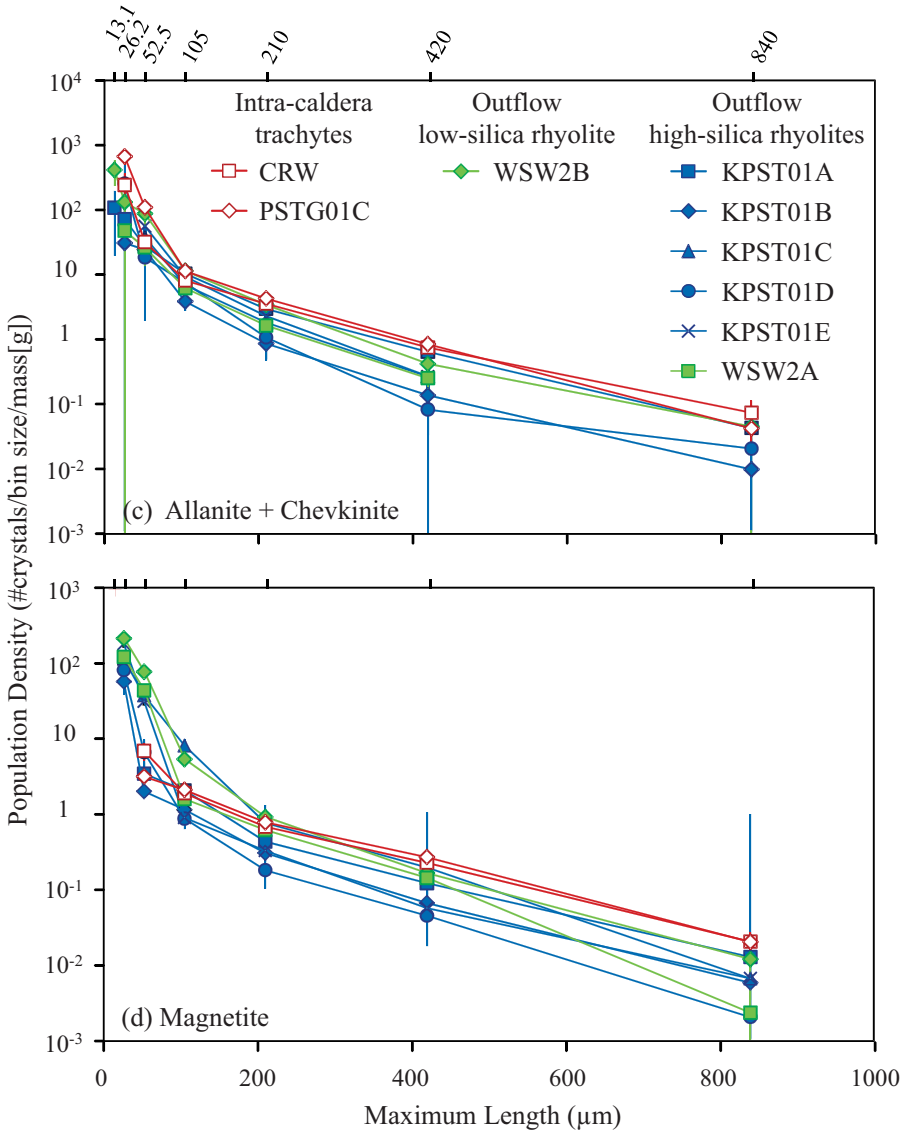

Fig. 11. Continued.

broad sense). Phenocryst assemblages are almost identical throughout, but late-erupted, presumably deeper-derived, trachytes are much richer in crystals, and in all elements compatible in them, than the earlier-erupted rhyolites. This applies not only to bulk pumice and fiamme but also to glass, and not only to elements that are notably enriched in trachyte, such as K, Zr, and REE, but also to feldspar-compatible Ba and Sr. Barium and Sr are not unusually high in the trachyte fiamme (~1000–3000 ppm and 200–400 ppm in bulk fiamme, respectively), but they are far higher than in the rhyolite pumice (~30–100 and 10–40 ppm). We expand on the hypothesis that the trachytic fiamme represent a remobilized crystal-enriched mush and that the rhyolite pumice was derived from a previously extracted, crystal-depleted magma in more detail below.

Cooling and crystallization in the high-silica portion of the Peach Spring magmatic system

Textures and compositional variations in accessory minerals from the high-silica rhyolites indicate a pre-eruptive history of relatively uninterrupted cooling and crystallization. In simply considering qualitative textural observations, there is support for such a simple history in that phenocrysts are typically euhedral and display pristine zoning (Figs 12 and 13). CSDs from the high-silica rhyolites are in agreement with this in that many are linear on

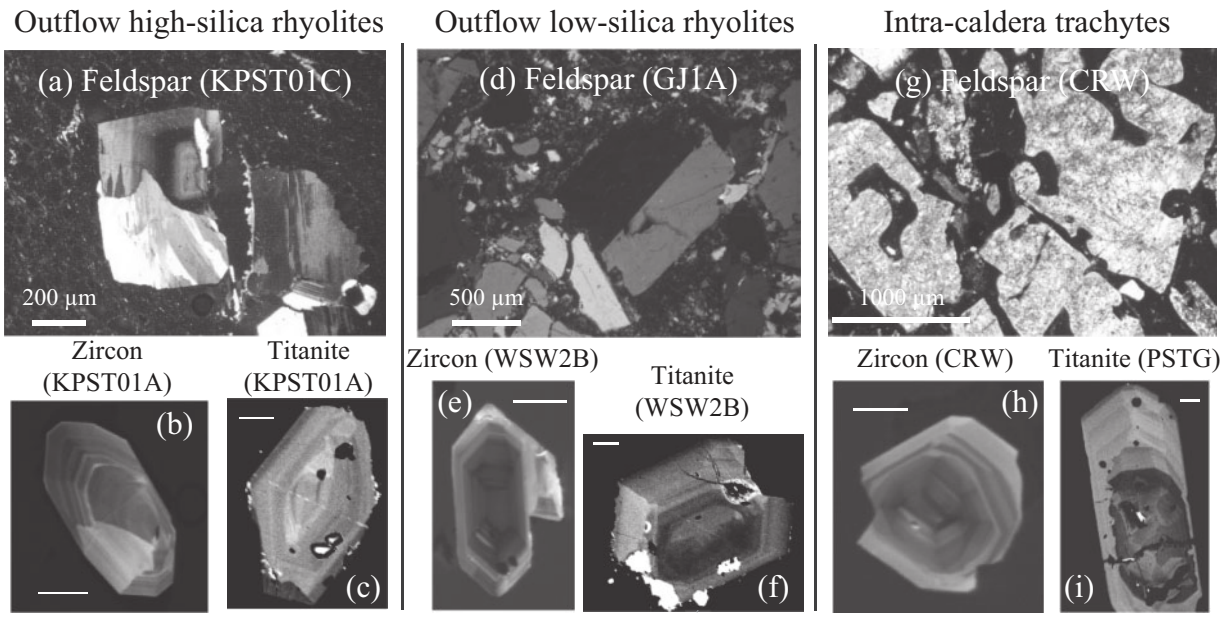

Fig. 12. Photomicrographs of thin sections and crystal separates from (a–c) outflow high-silica rhyolites, (d–f) outflow low-silica rhyolites, and (g–i) intra-caldera trachytes. Feldspar in thin sections (a, d, g), cathodoluminescence images of zircon crystals (b, e, h), and backscattered electron images of titanite crystals (c, f, i). Unless otherwise stated, scale bars represent 50 μm.

semi-log plots (see Results, Fig. 11), particularly for larger crystals, consistent with a single crystallization event during the pre-eruptive history. Furthermore, core-to-edge temperature trends in zircon and titanite from the high-silica rhyolites are consistent with the simple history revealed in the textural observations, as the rims record notably cooler temperatures than cores (Fig. 10). Although comparison of absolute temperatures retrieved from thermometry (uncertain owing to activities) and from rhyolite-MELTS (systematically high; see Gualda *et al.*, 2012*a*) is difficult, the temperature intervals recorded in zircon and titanite are in broad agreement with those derived from rhyolite-MELTS simulations of the high-silica rhyolite (Fig. 15).

Further evidence of simple differentiation of the system with crystallization is also found in the trace element variations (Figs 7 and 8). Crystallization of the observed accessory mineral assemblage, including zircon, allanite, chevkinite, and titanite, would yield qualitatively predictable elemental trends in REE and Zr/Hf in the evolving melt that would, in turn, leave identifiable signatures during continuing mineral growth. For example, LREE concentrations in allanite- or chevkinite-saturated melts decline as temperature falls and crystallization takes place, because the LREE are essential structural constituents in these minerals and saturation levels for these elements decline with falling temperature. Furthermore, although zircon incorporates abundant Hf, Zr is slightly preferred over Hf in the zircon–hafnium solid solution series (Linnen & Keppler, 2002), so Zr/Hf ratios fall in melts as zircon crystallizes (Claiborne *et al.*, 2006). Finally, titanite has extremely high partition coefficients for all the REE, but especially for the MREE, such that even small modal fractions of titanite result in compatible behavior of the REE and strong depletion of the MREE (Bachmann *et al.*, 2002; Glazner *et al.*, 2008; Colombini *et al.*, 2011). Thus, the relatively continuous core-to-edge depletion in REE contents with increasing Hf (in zircon) and decreasing Gd (in titanite) is indicative of fractionation by relatively uninterrupted growth of these accessory phases.

The compositions and textures of accessory minerals in the high-silica rhyolites also suggest that the onset and duration of crystallization of single accessory minerals differed. Zircon from the high-silica rhyolites records temperature intervals of at least 50°C, and possibly as large as 100–170°C, with the highest-Ti cores requiring temperatures in excess of 800°C. The variation in Zr contents in titanite is comparatively small, resulting in a temperature interval of titanite crystallization of <50°C, with crystallization temperatures below 770°C, possibly as low as 720°C. The depletion in MREE observed in zircon from the high-silica rhyolites suggests co-crystallization of zircon and titanite, showing that at least the zircon rims were growing within the magma body (i.e. as opposed to being antecrysts). This scenario of zircon crystallization over a wide temperature interval with titanite saturation occurring at lower temperatures and recording a narrower crystallization interval is consistent with what is seen in other silicic systems (e.g. Colombini *et al.*, 2011).

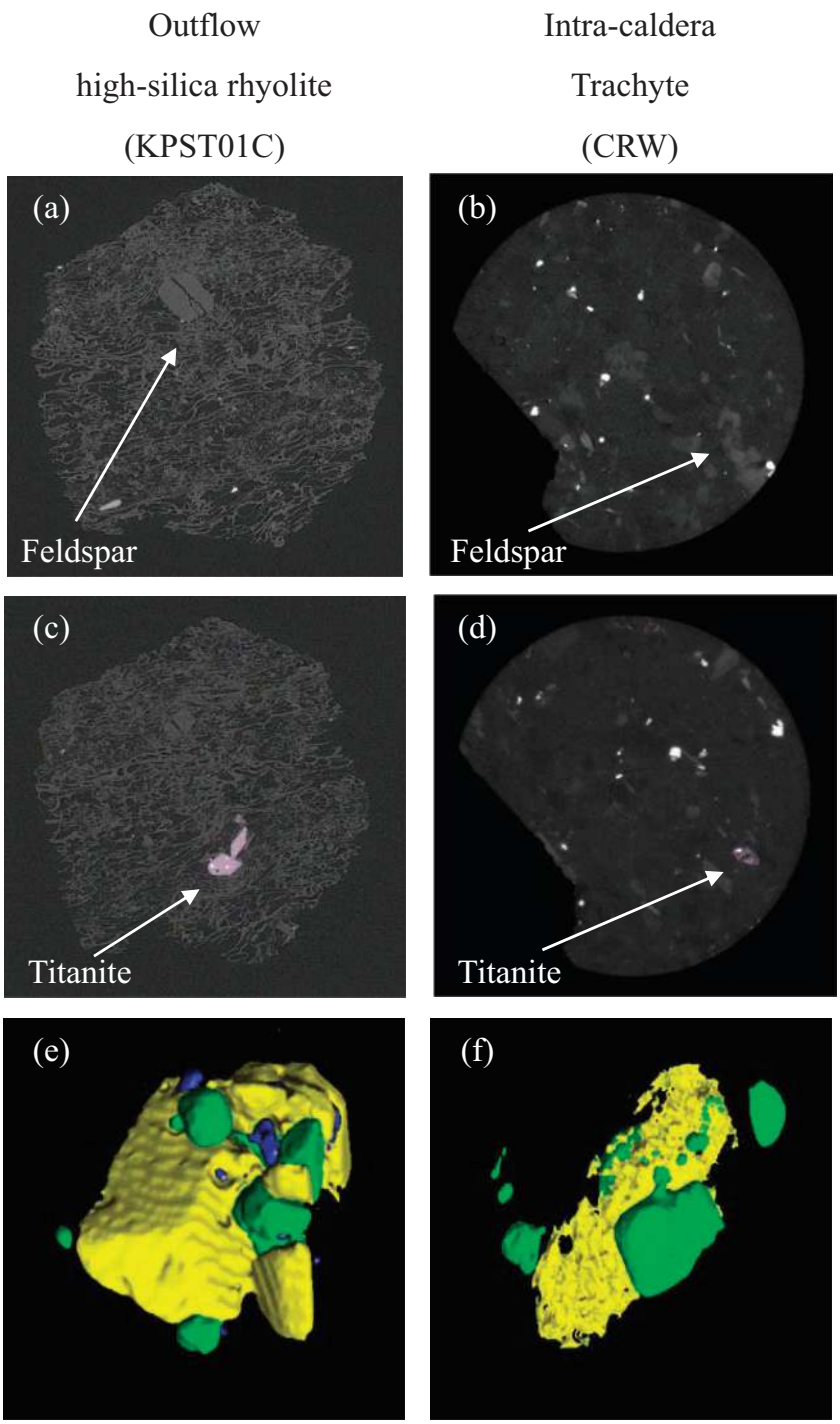

Fig. 13. Tomographic images and 3D renditions of phenocrysts from (a, c, e) outflow high-silica rhyolite (KPST01C), and (b, d, f) intra-caldera trachyte (CRW). White (yellow in online version of figure) is titanite, light gray (green online) is magnetite, dark gray (blue online) is zircon. Field of view is 1·2 cm wide in (a)–(d) and 1·1 mm wide in (e) and (f).

Texturally, the prevalence of accessory minerals (magnetite, titanite, allanite + chevkinite, and zircon) as clusters rather than as independent crystals (Fig. 14) is notable and suggests that not only was crystallization of these phases relatively contemporaneous, but that crystallization of one accessory phase may have facilitated growth of the others (e.g. Bacon, 1989). These results imply that whereas the onset of growth of these phases differed and zircon

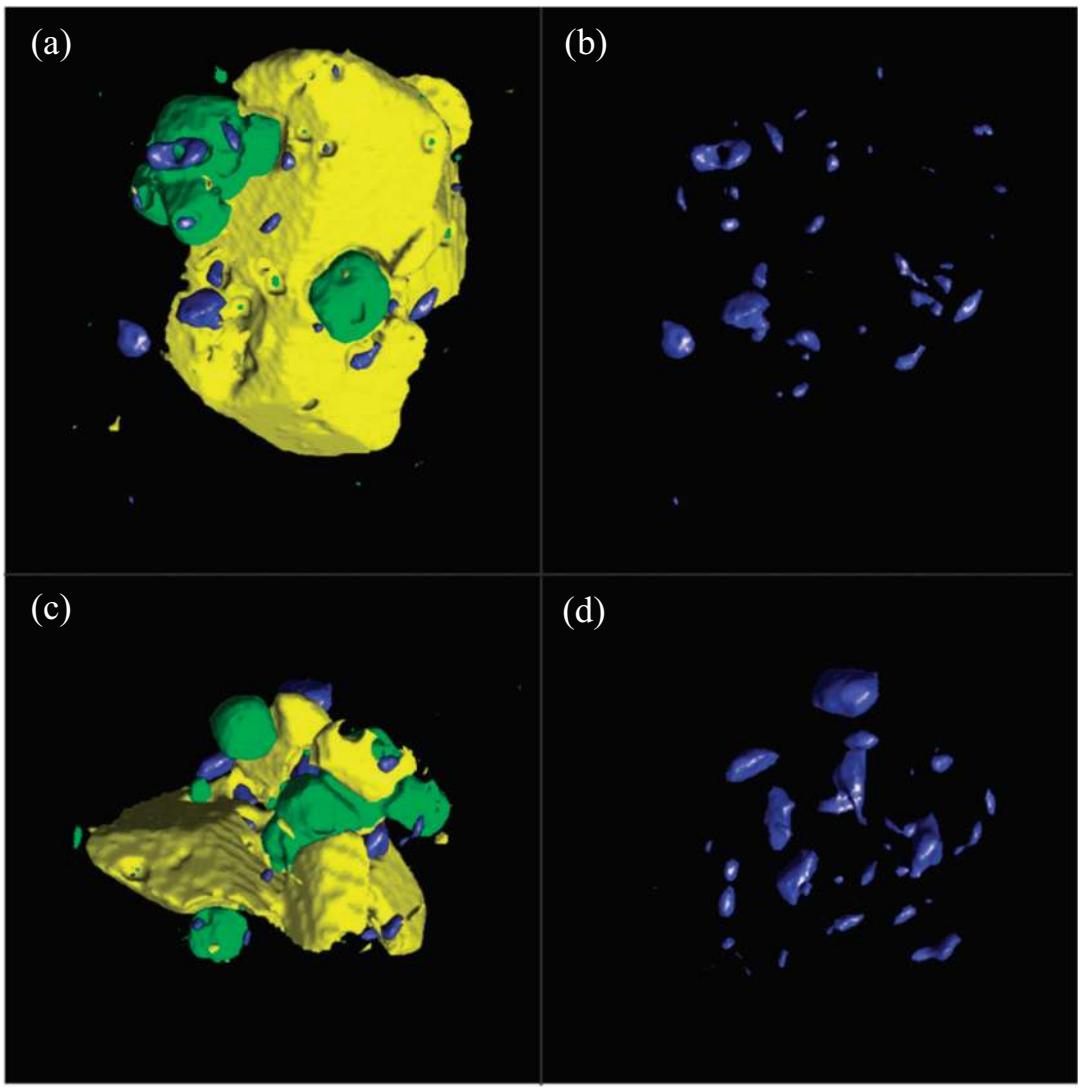

Fig. 14. Three-dimensional rendition of accessory minerals in an outflow high-silica rhyolite pumice clast (KPST01C). White (yellow in online version of figure) is titanite, light gray (green online) is magnetite, dark gray (blue online) is zircon. (a, c) Three-dimensional renditions including titanite, zircon, and magnetite clustered together. (b, d) Same images as (a, c) with titanite and magnetite hidden. It is clear in these images that zircon is preferentially clustering with other accessory minerals. Field of view is 1.1 mm wide. (To see an animated version of this image, see Supplementary Data Electronic Appendix 2.)

saturated at a considerably higher temperature than titanite, the bulk of their crystallization was coeval, in agreement with the geochemical evidence.

Heating in the Peach Spring Tuff chamber

The textures and compositions of accessory minerals in the Peach Spring trachytes reveal an additional facet of the history of the Peach Spring magmatic system. First, the trace element compositions of titanite provide compelling evidence that an influential event occurred between the time of core and edge crystallization. Unlike in the high-silica rhyolites, the edges of the titanite crystals in the trachyte are significantly enriched in REE relative to the cores (Fig. 6), signifying that this event replenished the REE content of the melt. There is a marked increase in the MREE in particular, which suggests that this event replenished the MREE contents more than the LREE and HREE contents of the system. Release of REE into the melt by resorption of zircon, titanite, and allanite + chevkinite is a possible mechanism to explain these REE enrichments, and textures provide evidence that this was the case.

Thin sections, crystal separates, and tomograms of the trachytes all reveal extensively resorbed feldspar, titanite, and zircon (Figs 12d, e and 13 b, d, f). The 3D reconstruction of a sieve-like remnant of titanite in CRW (Fig. 14) is

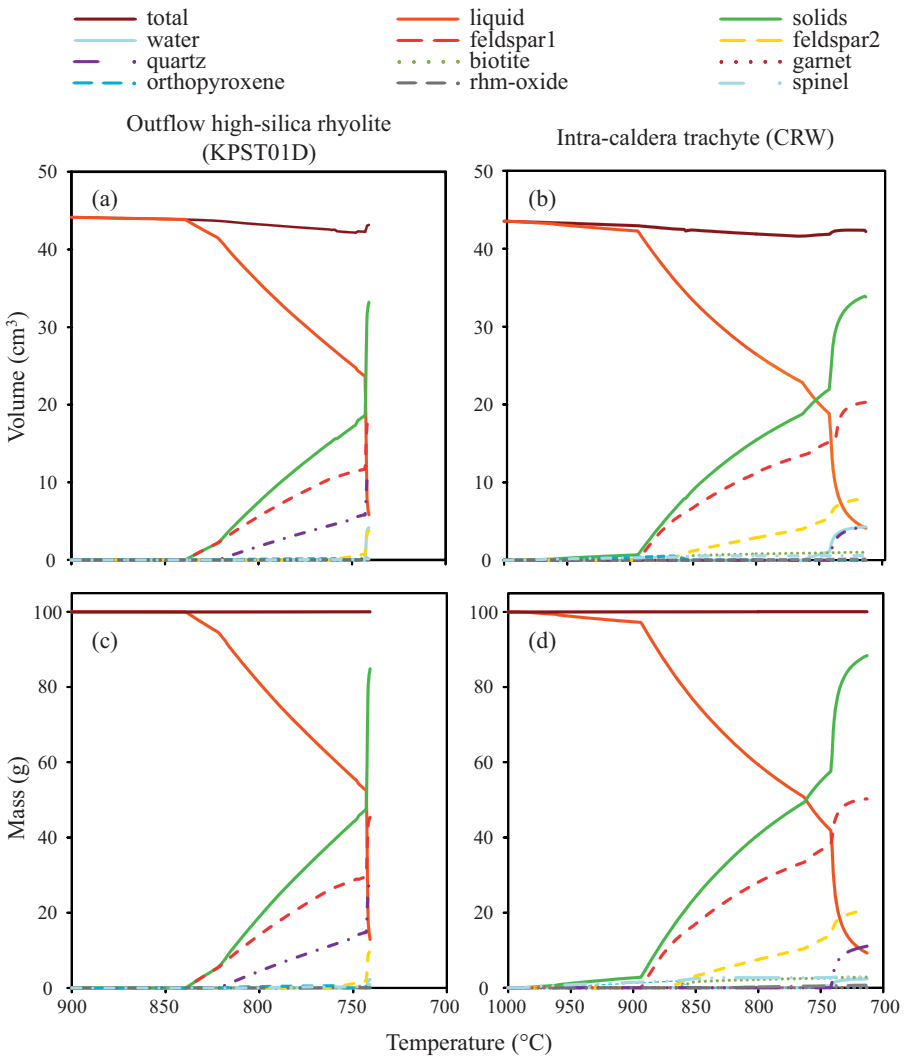

Fig. 15. Examples of rhyolite-MELTS simulations showing volume and mass vs temperature, for (a, c) an outflow high-silica rhyolite (KPST01D) and (b, d) an intra-caldera trachyte (CRW) composition at 250 MPa and 3 wt % water. Rhm-oxide: rhombohedral oxide.

particularly striking. Although the separated zircons are rounded, they do not appear to have the same sieve-like textures as the titanite grains; they remain relatively abundant in the trachytes, whereas titanite was not even found in the CRW separates. This suggests that resorption of titanite was more extensive than zircon resorption, which is consistent with especially strong enrichment in the MREE in rims. Zircon textures and compositions are consistent with resorption and accompanying development of reaction rims equilibrated with an evolving melt that was still zircon-saturated.

CSDs are also consistent with the resorption of accessory phases in general, and of titanite in particular (Fig. 11b). First, population densities of large titanite crystals in trachytes are considerably lower than those of other accessory phases, probably because titanite was resorbed more extensively than the other phases. Furthermore, whereas titanite size distributions are kinked as in the rhyolites, the distributions for small crystals in the trachytes are distinctively concave-down. It is possible that the titanite size distributions in the trachytes were originally (at least qualitatively) similar to those of the rhyolites, but were subsequently modified by preferential resorption of small titanite crystals.

One way to cause resorption of crystals is heating, and there is evidence in our data in support of a heating event. The crystallization interval for titanite in the trachytes is ~30°C (Fig. 9c and d); again, much smaller than that for zircon. Temperatures recorded in zircon and titanite edges are generally higher than in cores and interiors in the trachytes, suggesting that the system was heated at some point between interior and edge crystallization (Fig. 9). Titanite rims record much lower temperatures than zircon rims (740–780°C in titanite, as compared with

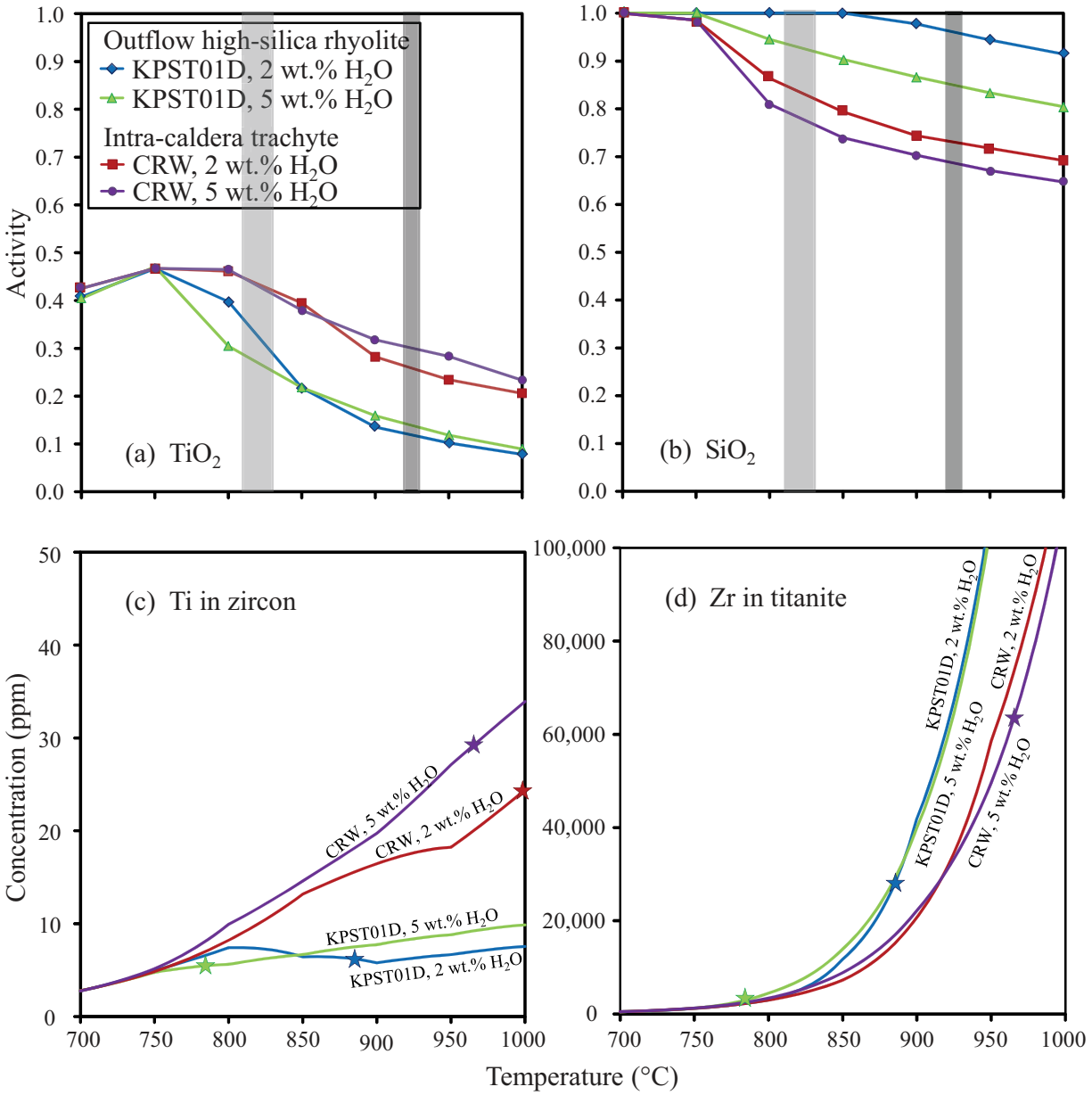

Fig. 16. Plots of Temperature vs. (a) TiO_2 activity, (b) SiO_2 activity, (c) Ti contents in zircon, and (d) Zr content in titanite. Activity values were calculated from rhyolite-MELTS simulations for an outflow high-silica rhyolite (KPST0lD) and an intra-caldera trachyte (CRW) with variable water contents (2 or 5 wt %). Ti in zircon and Zr in titanite for any given temperature are the equilibrium concentrations calculated using the corresponding activities from rhyolite-MELTS. Temperatures can be read from the bottom diagrams (c) and (d) if measured concentrations are known. Light and dark gray shaded regions in (a) and (b) indicate bulk pumice and fiamme zircon saturation temperatures from outflow high-silica rhyolites and intra-caldera trachytes, respectively. Stars indicate liquidus temperatures.

>~900°C in zircon), which is consistent with the evidence for substantial titanite resorption and with the narrower crystallization interval of titanite.

The titanium contents of zircon edges are extremely high and suggest maximum edge temperatures of zircon >~900°C in intra-caldera fiamme. To achieve such temperatures, an influx of a significant amount of heat is required (Huber *et al.*, 2010). The presence of trachyandesite magmatic enclaves in the Peach Spring Tuff, although rare, suggests that a more mafic magma input may have provided the heat necessary to raise the temperature to the observed levels. However, a far greater volume of relatively mafic magma than that observed as enclaves in the Peach Spring Tuff would be required to accomplish the amount of heating that is evident in the trachyte. Therefore, for this to be a viable mechanism,

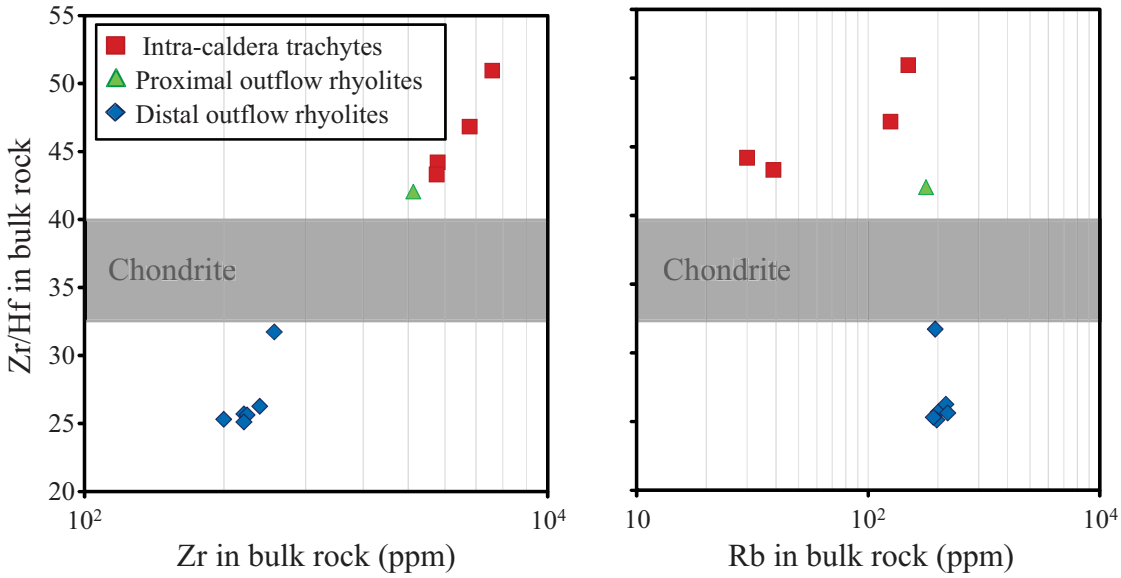

Fig. 17. Zr/Hf vs (a) Zr and (b) Rb in proximal outflow rhyolites, distal outflow rhyolites, and intra-caldera trachyte.

most of the mafic magma input would have to have been trapped somewhere else, presumably deeper within the system, and not erupted (e.g. mafic underplating; e.g. Couch *et al.*, 2001).

Importantly, the textures and compositions of the low-silica rhyolites (both WSW2B and GJ1A) are notably different from those of the high-silica rhyolites and trachytes. Interestingly, trace element trends in WSW2B are similar to those in the trachytes and are also suggestive of a heating event, but the textures show little to no indication of resorption and are much more akin to those of the high-silica rhyolites, which do not show geochemical evidence of heating. In contrast, GJ1A shows more extreme textural evidence for heating, but it is more similar to the high-silica rhyolites geochemically. Consequently, these samples suggest that, although the effects of heating were not felt by the entire system, they were also not restricted to the magmas that yielded the trachytic intra-caldera tuff.

Evidence for crystal accumulation and subsequent remobilization of the cumulate

A number of observations from mineral textures, the compositions of bulk pumice and fiamme, glasses and zircon crystals provide evidence to suggest that the intra-caldera deposits may be remobilized cumulates from the Peach Spring magma chamber.

First, the trachytes have cumulate-like compositions: the fiamme compositions are unusual for a magma in that they are extremely rich in feldspar components and the accessory mineral constituents Zr, P_2O_5, and REE (e.g. ~80% normative feldspar, up to ~800 ppm Zr, 0·2 wt % P_2O_5, and near 200 ppm La). These compositions are consistent with the trachyte phenocryst mineralogy and suggest that the trachytes are accumulations of the feldspar and an accessory mineral assemblage that is characteristic of both the intra-caldera and outflow tuff. The trace-element compositions of the trachytes and high-silica rhyolites are consistent with expectations for cumulates and extracted melts, respectively (Deering & Bachmann, 2010; Fig. 17). Second, the trachytes are characterized by abundant phenocrysts: despite clear evidence of phenocryst dissolution (Figs 12 and 13), the intra-caldera trachyte fiamme are crystal rich. Thorson (1971) estimated an average of 35% phenocrysts in the trachyte tuff, consistent with our own observations. The evidence for dissolution suggests that the trachyte magmas were originally significantly more crystal rich. The outflow pumice is generally phenocryst poor (~4–14%, Young & Brennan, 1974). Finally, as noted above in the discussion, there is ample evidence for a late high-temperature event in the zircon saturation temperatures, Ti concentrations of zircon edges, Zr and REE contents of titanite edges, and quantitative and qualitative textural features.

These observations are consistent with, or directly support, a model in which the crystal-rich base of the Peach Spring magma chamber was heated and its melt fraction was increased substantially, serving to remobilize a nearly or entirely 'locked-up' mush or rigid sponge (Hildreth, 2004). This interpretation is consistent with those for similar phenocryst-rich volcanic rocks that accompany crystal-poor rhyolites, such as at the Ossippee ring dike complex (Cretaceous, New Hampshire) by Kennedy & Stix (2007), the Timber Mountain caldera complex (Miocene, Nevada) by Bindeman & Valley (2003), and

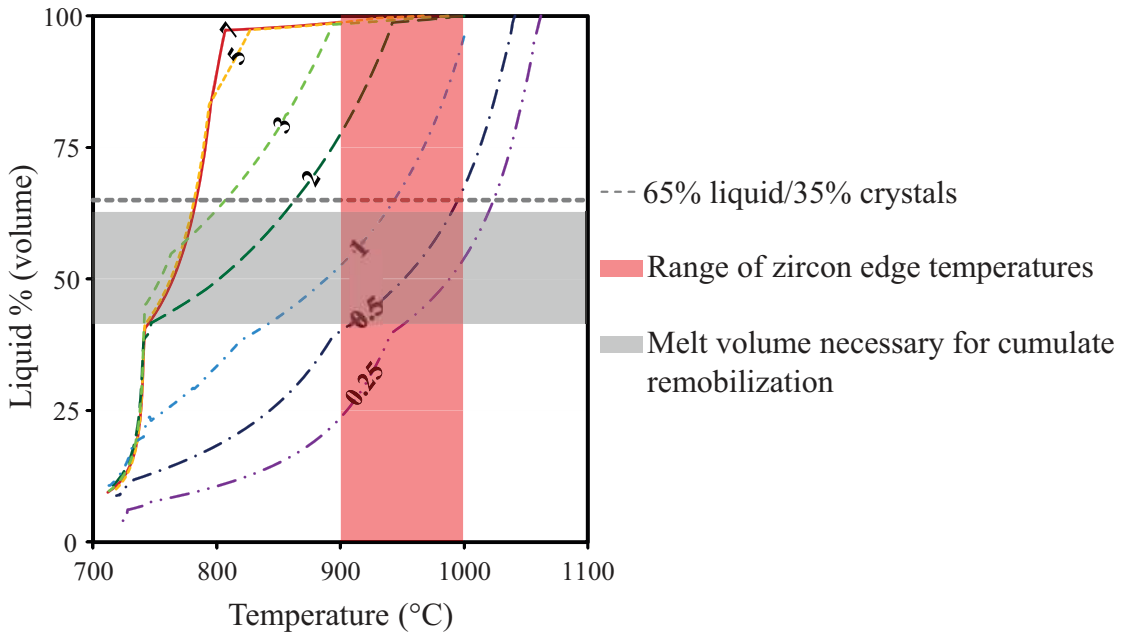

Fig. 18. Temperature vs liquid % (by volume) from rhyolite-MELTS simulations at variable water contents for a trachyte composition (CRW). Bulk water contents (wt % H_2O) for each simulation are indicated by the bold numbers on each line. Range of possible maximum temperature based on Ti-in-zircon and zircon saturation thermometry (dark gray field; red in online version of figure) and approximate melt (glass) content of the sample (65%, gray dashed line) are shown; their intersection represents the CRW magmatic conditions at the time of eruption, including the bulk water content of the magma. Evolution of the magma would follow an appropriate path determined by the bulk water content. The light gray field denotes the conditions of transition from 'locked rigid sponge' to mobile magma.

the Ammonia Tanks Tuff (Miocene, Nevada) by Deering *et al.* (2011). Those researchers also argued for late-stage mobilization of syenite and monzonite cumulates during giant rhyolite eruptions.

Furthermore, the intra-caldera tuff erupted after the caldera collapse, presumably after emplacement of the outflow. Consequently, the simplest interpretation of the pre-eruption magma chamber geometry is that the intra-caldera tuff represents deep levels (last evacuated) and that the outflow is from the upper portion of the chamber. This is consistent with the higher temperatures evidenced by the intra-caldera tuff and with its apparent cumulate nature.

Unlocking the cumulate

Combining our observations with rhyolite-MELTS modeling, we can place some important constraints on this model of an 'unlocked' cumulate. If the trachytes are indeed melt-depleted cumulates that were partially remelted after accumulation, then rhyolite-MELTS simulations do not pertain to the crystallization process, but rather to the melting process; the simulations are appropriate for the melting process, assuming that little phase fractionation was imposed. Under the assumption that the trachyte was remobilized in bulk, the water contents of the total system can be assessed using the phase relations derived from rhyolite-MELTS (Fig. 18). Given the constraints that the temperature of the trachyte magma reached at least ~900–950°C (as indicated by zircon rims) and that the melt fraction was ~65% (given 35% crystal contents), the simulations suggest that the total water content of the trachytes was ~1 wt % (see Fig. 18); this is a conservative estimate—that is, water contents could have been even lower—given that temperatures could be higher (see above). These constraints allow us to consider two important questions about the cumulate, as follows.

(1) Did the Peach Spring magma ever exist under subsolidus conditions? If the cumulate corresponds to accumulations of the phenocryst assemblage characteristic of the outflow, 5–10% of the crystals might comprise biotite and hornblende combined; considering that hornblende and biotite have ~2–4 wt % H_2O, the total water that could be held by a totally solid cumulate is 0·2–0·4 wt %. This is substantially less than our estimate of 1 wt % H_2O. It follows that either H_2O was supplied to the system during melting, or melt—capable of holding up to ~5·5 wt % dissolved H_2O at a likely pressure of 250 MPa (saturation level), obtained from rhyolite-MELTS simulations—was present during reheating. If volatiles were supplied by mafic magma, they would tend to be relatively CO_2-rich, and mixing with H_2O-rich

volatiles characteristic of the rhyolitic magma would lead to crystallization, rather than melting. Rejuvenation by felsic magmas could provide H_2O-rich fluids, but we see no evidence for this process, and in any case it could not provide the heat required to achieve the estimated peak temperatures. We conclude that the simplest way to account for the water necessary for melting is for the cumulate to have been above its solidus, always retaining some fraction of melt.

(2) What percentage of the cumulate was melted in the process of heating and remobilization? It is likely that the melt that was trapped in the cumulate prior to heating was at or near water saturation (~5·5 wt % water). If it is assumed that the cumulate was mobilized *en masse*, that the cumulate as a whole contained 1 wt % water (see estimate of trachyte water content above), and that all the water resided in the melt, then the melt fraction in the cumulate prior to heating was ~15–20% (H_2O in melt ÷ total H_2O). Thus, the cumulate was an immobile 'rigid sponge' (Hildreth, 2004). Again assuming *en masse* mobilization, close to 50 wt % of the cumulate was melted in the heating and remobilization process (65 wt % melt in the trachyte − 20 wt % melt in the pre-heating magma). It should be noted, however, that if melt was preferentially extracted, instead of being remobilized *en masse*, both the amount of the initial melt and the extent of subsequent melting would have been lower.

Timescales of crystallization and eruptive decompression

Timescales of crystallization calculated from CSDs can place useful constraints on the longevity of a magmatic system and the onset of eruption (Cashman & Marsh, 1988; Mangan, 1990; Jerram *et al.*, 2003). The kinked titanite and magnetite CSDs observed here (Fig. 11d), with a shallow-sloped section characteristic of large crystals and a steep-sloped section characteristic of small crystals (<100 μm), are in many ways analogous to quartz + feldspar CSDs for the late-erupted Bishop Tuff (Pamukcu *et al.*, 2012). As such, we likewise attribute this change in slope to a record of the transition from pre-eruptive, growth-dominated crystallization to syn-eruptive, nucleation-dominated crystallization, similar to what is seen in smaller volcanic systems (e.g. Cashman, 1988, 1992; McCanta *et al.*, 2007).

Each of the segments of the size distributions records a characteristic crystallization timescale, which can be calculated if relevant growth rates are known. CSDs can be used to estimate the growth time of a given phase from the relationship $t = 1/Gb$ (Marsh, 1988, 1998), where t is growth time, G is the linear growth rate, and b is the slope of the CSD in semi-log space. The main barrier to application of this approach is the fact that growth rates are poorly known. For instance, there is almost no information on titanite growth rates, so timescales of titanite crystallization cannot be calculated.

Magnetite phenocryst and groundmass growth rates can be estimated from data on the Mount St. Helens dacite (Cashman, 1988, 1992). Cashman (1988) estimated a phenocryst growth rate of 10^{-14}–10^{-15} m s^{-1} for Fe–Ti oxides, based on an estimated growth time of 50–130 days. Although some plagioclase crystal cores yield ages of up to 1700 years (Cooper & Reid, 2003), these are likely to represent antecrysts; more recent work suggests that much of the phenocryst growth actually occurred rapidly near the time of eruption, making these earlier estimates of phenocryst growth rates minimum estimates (Blundy & Cashman, 2005). Consequently, timescale estimates based on these growth rates are maximum estimates. Growth rates for Fe–Ti oxide microlites are not as well constrained, but we use the estimated period of groundmass growth of 1 h to 52 days in the Mount St. Helens dacites, and the fact that the groundmass magnetite crystals are <0·1 μm in size (for details, see Cashman, 1992), to calculate magnetite microlite growth rates of 10^{-12}–10^{-14} m s^{-1}; we note that these are maximum estimates of the relevant growth rates, given that the size of the magnetite microlites in the Mount St. Helens dacites could actually be substantially smaller than 0·1 μm, and the resulting calculated crystallization times are thus minimum estimates. Nonetheless, we see no reason for groundmass growth rates to be any slower than those for phenocrysts; instead, we expect growth rates to increase with decompression (see Cashman, 1992), owing to the resulting increase in supersaturation, such that we use a maximum groundmass growth rate of 10^{-14} m s^{-1}.

Applying these growth rates to magnetite size distributions from the Peach Spring Tuff, we estimate timescales of magnetite growth (Table 7) for the two segments of the kinked magnetite CSD. Results suggest that the large crystal population (>100 μm) in the Peach Spring Tuff grew in hundreds to thousands of years. These timescales are overestimates if the largest crystals are antecrystic or xenocrystic in origin. These results are in agreement with those obtained for the Bishop Tuff by Pamukcu *et al.* (2012) using quartz + feldspar CSDs, and by Gualda *et al.* (2012*b*) using relaxation of Ti profiles and faceting of melt inclusions in quartz. They lend further support to the conclusion of Gualda *et al.* (2012*b*) that giant bodies of rhyolitic magma crystallize on millennial timescales, whereas the protracted timescales recorded in zircon record the build-up of these giant crystal-poor magma bodies.

The small magnetite population (<100 μm) of the Peach Spring rhyolites yields crystallization times between 0·1 year and a few hundred years prior to eruption (at growth rates of 10^{-12}–10^{-14} m s^{-1}). Given our expectation that growth rates should increase with decompression, we

Table 7: Timescales of magnetite crystallization

	Small crystals							
	Outflow high-silica rhyolites					Outflow low-silica rhyolite	Intra-caldera trachytes	
	KPST01A	KPST01B	KPST01C	KPST01E	WSW2A	WSW2B	PSTG01C	CRW
$-1/Gt$	−0·0097	−0·0359	−0·0547	−0·0673	−0·0561	−0·0474	−0·0089	−0·0246
Gt (μm)	103	27·9	18·3	14·9	17·8	21·1	112	40·7
t (a) short*	0·33	0·09	0·06	0·05	0·06	0·07	0·36	0·07
t (a) long†	327	88·3	58·0	47·1	56·5	66·9	356	130

	Large crystals							
	KPST01A	KPST01B	KPST01C	KPST01E	WSW2A	WSW2B	PSTG01C	CRW
$-1/Gt$	−0·0056	−0·0069	−0·0076	−0·006	−0·009	−0·0068	−0·0062	−0·0056
Gt (μm)	179	145	132	167	111	147	161	179
t (a) short‡	566	460	417	528	352	466	511	566
t (a) long§	5660	4600	4170	5280	3520	4660	5660	5110

G, growth rate; t, time.
*Growth rate of 10^{-12} m s^{-1}, based on groundmass Fe–Ti oxide sizes and growth times from Cashman (1992) (see text for details).
†Growth rate of 10^{-15} m s^{-1}, based on groundmass Fe–Ti oxide sizes and growth times from Cashman (1992) (see text for details).
‡Growth rate of 10^{-15} m s^{-1}, based on phenocryst Fe–Ti oxide growth rates from Cashman (1988) (see text for details).
§Growth rate of 10^{-16} m s^{-1}; based on phenocryst Fe–Ti oxide growth rates from Cashman (1988) (see text for details).

infer that growth times are closer to 0·1 year than to the other end of the time spectrum. If, as suggested, the growth of this population of small crystals was the result of eruptive decompression, this suggests that decompression began within months to years before eruption; these results are also in good agreement with those of Gualda (2007) and Pamukcu *et al.* (2012) for the Bishop Tuff.

These results also suggest that the heating and decompression events may have been associated. The textural and geochemical evidence implies that both events occurred close to the time of eruption. Furthermore, heating of a magmatic system by a mafic recharge event has been suggested as a possible eruptive trigger (Sparks *et al.*, 1977; Pallister *et al.*, 1992), destabilizing the magma body by reducing its density and viscosity through processes such as overturning, increasing fluid pressure by increasing volume, bubble growth and vesiculation. Consequently, if input of mafic magma and heating of the Peach Spring magma body did act as an eruption trigger, decompression of the system would naturally follow as the eruptive process began.

Interestingly, such kinks are not found in zircon and allanite + chevkinite CSDs, but this may merely be due to a difference in growth rates. There is much interest in determining zircon growth rates (Watson, 1996; Reid, 2008; Schmitt *et al.*, 2011). Modeling of diffusion-controlled growth is consistent with growth rates in the range 10^{-15}–10^{-19} m s^{-1} (Watson, 1996). Recent work on the Acigöl rhyolite field (Central Anatolia; Schmitt *et al.*, 2011) has revealed a simple zircon crystallization history conducive to making reliable zircon growth rate estimates using dating methods; the results yield average growth rates in the range 10^{-15}–10^{-16} m s^{-1} (with a preferred value of 3×10^{-16} m s^{-1}), at the faster end of the range given by modeling. Application of these growth rates to the CSD segments defined by zircon crystals larger than 100 μm gives timescales of zircon growth in the range 1800–27 000 years (Table 8), with values of 6000–9000 years for the preferred growth rate of 3×10^{-16} m s^{-1} of Schmitt *et al.* (2011). We consider these results to agree well with the magnetite phenocryst growth rates calculated above, particularly considering the greater likelihood of xenocrystic and antecrystic zircon when compared with magnetite. In any event, the reasonable agreement between zircon and magnetite growth times suggests that most of the zircon mass is cognate with the other phenocrysts, with cores—albeit important—making up a small proportion of the total volume. Because zircon growth is substantially slower

Table 8: Timescales of zircon crystallization

	Large crystals							
	Outflow high-silica rhyolites					Outflow low-silica rhyolite	Intra-caldera trachytes	
	KPST01A	KPST01B	KPST01C	KPST01E	WSW2A	WSW2B	PSTG01C	CRW
$-1/Gt$	−0·017	−0·012	−0·013	−0·014	−0·017	−0·014	−0·017	−0·013
Gt (μm)	58	85	75	73	60	70	60	77
t (a) short*	1883	2691	2382	2306	1902	2225	1900	2426
t (a) long†	18330	26911	23815	23059	19015	22249	19003	24258

G, growth rate; t, time.
*Growth rate of 10^{-15} m s^{-1}, from Schmitt *et al*. (2011) (see text for details).
†Growth rate of 10^{-16} m s^{-1}, from Schmitt *et al*. (2011) (see text for details).

than magnetite growth, zircon crystals nucleated owing to a decompression event near the time of eruption probably did not have enough time to grow to a resolvable size (~10 μm) before eruption, thereby not recording the event on the length scales currently being described.

CONCLUSIONS

Our study of the Peach Spring magma body, based on the compositions and textures of bulk samples, glasses, and accessory minerals from outflow and intra-caldera pumice and fiamme, in combination with rhyolite-MELTS modeling, reveals an intriguing evolution of this system.

(1) The Peach Spring magma body was zoned. This is indicated by a systematic variation in crystal contents, bulk pumice and fiamme compositions, spatial distributions, and temperatures recorded in accessory mineral phases; crystal-poor high-silica rhyolites in the more distal outflow record the lowest temperatures, whereas intra-caldera crystal-rich trachytes record the highest temperatures.

(2) The high-silica portion of the Peach Spring magma body followed a relatively simple history of cooling and crystallization. Core-to-edge depletion in REE in zircon and titanite crystals, as well as core-to-edge decreases in Ti in zircon and Zr in titanite contents, suggests crystal growth during largely uninterrupted cooling. Trends in REE indicate co-crystallization of accessory minerals, although zircon records a more protracted growth history than titanite. Exponential CSDs and qualitative textural features (e.g. euhedral phenocrysts, pristine zoning) are consistent with the geochemical evidence. Crystallization intervals derived from rhyolite-MELTS simulations are also broadly consistent with the temperatures recorded in the high-silica rhyolites.

(3) A late-stage heating event in the Peach Spring magma body may have contributed to the onset of eruption. In trachytes and low-silica rhyolite, the edges of titanite crystals show enrichment in REE and Zr, and zircon edges are enriched in Ti, suggesting higher temperatures during edge crystallization. Concave-down portions of CSDs characteristic of small crystals, embayed feldspars, and sieve-like titanite crystals in the trachytes also suggest resorption of phenocrysts, consistent with this increase in temperature. The fact that phenocrysts in the low-silica rhyolite and the high-silica rhyolites show little to no textural evidence for the heating event implies that this event did not affect the entire Peach Spring magma body to the same extent.

(4) The trachytes represent remobilized cumulates, but this magma was never fully crystalline. The bulk fiamme compositions of the trachytes are extremely rich in feldspar and accessory mineral components, indicating that these rocks represent accumulations of the phenocryst assemblage that characterizes the Peach Spring Tuff. The abundance of phenocrysts and evidence for heating and resorption in the trachytes also suggest that the magma from which these samples came was originally more crystal rich. Rhyolite-MELTS simulations suggest that the cumulate had ~1 wt % water and that hydrous phases cannot account for this amount of water if the cumulate were fully crystalline, suggesting that the cumulate included some proportion (~20 wt %) of melt. These simulations also suggest that ~50% of the cumulate was melted during the reheating process.

(5) Crystal size distributions indicate that the Peach Spring magma body crystallized over millennial timescales and record the onset of eruptive decompression. Growth rates for magnetite crystals and

slopes of magnetite crystal size distributions suggest that the phenocrysts of the Peach Spring Tuff grew over 10^3–10^4 years, whereas the groundmass crystals grew over 10^{-1}–10^2 years. Kinks in magnetite crystal size distributions are attributed to a decompression event, which changed the crystallization regime from growth-dominated (shallow slopes describing large crystals) to nucleation-dominated (steep slopes describing small crystals). Timescales calculated from zircon size distributions are consistent with those obtained from magnetite, and suggest that much of the zircon growth occurred concurrent with the growth of other phenocrysts.

ACKNOWLEDGEMENTS

We are grateful to M. Ghiorso, M. Rivers, J. Wooden, K. Cashman, and D. Buesch for helpful and insightful discussions as we developed and revised this work. We also thank A. Schmitt, two anonymous reviewers, and editor W. Bohrson for thorough and helpful reviews. Discussions with and data shared by David Buesch, Jonathan Miller, Susanne McDowell, Bill McIntosh, and Reba McCracken provided useful insights into the Peach Spring eruption and magma system.

FUNDING

This work was funded by NSF grants EAR-0911726 (to C.F.M.) and EAR-0948528 (to G.A.R.G.). Portions of this work were performed at GeoSoilEnviroCARS (Sector 13), Advanced Photon Source (APS), Argonne National Laboratory; GeoSoilEnviroCARS is supported by the National Science Foundation–Earth Sciences (EAR-1128799) and Department of Energy–Geosciences (DE-FG02-94ER14466); use of the Advanced Photon Source was supported by the US Department of Energy, Office of Science, Office of Basic Energy Sciences, under Contract No. DE-AC02-06CH11357.

SUPPLEMENTARY DATA

Supplementary data for this paper are available at *Journal of Petrology* online.

REFERENCES

Bachmann, O. & Bergantz, G. W. (2003). Rejuvenation of the Fish Canyon magma body: A window into the evolution of large-volume silicic magma systems. *Geology* **31**, 789–792.

Bachmann, O. & Bergantz, G. W. (2004). On the origin of crystal-poor rhyolites: Extracted from batholithic crystal mushes. *Journal of Petrology* **45**, 1565–1582.

Bachmann, O., Dungan, M. A. & Lipman, P. W. (2002). Insights into shallow magmatic processes in large silicic magma bodies: the trace element record in the Fish Canyon magma body, Colorado. *Contributions to Mineralogy and Petrology* **149**, 338–349.

Bacon, C. R. (1989). Crystallization of accessory phases in magmas by local saturation adjacent to phenocrysts. *Geochimica et Cosmochimica Acta* **53**, 1055–1066.

Bacon, C. R. & Druitt, T. H. (1988). Compositional evolution of the zoned calcalkaline magma chamber of Mount Mazama, Crater Lake, Oregon. *Contributions to Mineralogy and Petrology* **98**, 224–256.

Billingsley, G. H., Weinrich, K. J., Huntoon, P. W. & Young, R. A. (1999). *Breccia-Pipe and geologic map of the southwestern part of the Hualapai Indian Reservation and vicinity, Arizona. USGS Miscellaneous Investigations Series Map I-2554* .

Bindeman, I. N. (2005). Fragmentation phenomena in populations of magmatic crystals. *American Mineralogist* **90**, 1801–1815.

Bindeman, I.N. & Valley, J.W. (2002). Oxygen isotope study of the Long Valley–Glass Mountain magmatic system, California: Isotope thermometry and convection in large silicic magma bodies. *Contributions to Mineralogy and Petrology* **144**, 185–205.

Bindeman, I.N. & Valley, J.W. (2003). Rapid generation of both high- and low-$\delta^{18}O$, large-volume silicic magmas at the Timber Mountain/Oasis Valley caldera complex, Nevada. *Geological Society of America Bulletin* **115**, 581–595.

Blundy, J. & Cashman, K. (2001). Ascent-driven crystallization of dacite magmas at Mount St. Helens, 1980–1986. *Contributions to Mineralogy and Petrology* **140**, 631–650.

Blundy, J. & Cashman, K. (2002). Petrologic reconstructions of magmatic system variables and processes. *Reviews in Mineralogy and Geochemistry* **69**, 179–239.

Blundy, J. & Cashman, K. (2005). Rapid decompression-driven crystallization recorded by melt inclusions from Mount St. Helens volcano. *Geology* **33**, 793–796.

Buesch, D. C. (1992). Incorporation and redistribution of locally derived lithic fragments within a pyroclastic flow. *Geological Society of America Bulletin* **104**, 1193–1207.

Buesch, D. C. & Valentine, G. A. (1986). Peach Springs Tuff and volcanic stratigraphy of the southern Cerbat Mountains, Kingman, Arizona. In: Nielson, J. E. & Glazner, A. F. (eds) *Cenozoic Stratigraphy, Structure and Mineralization in the Mojave Desert*. Los Angeles, CA: California State University, pp. 7–14.

Carley, T. L. (2010). Studies of the evolution of felsic magma systems: I. Zircon in historic eruptions, Iceland; II. Modeling magma chamber evolution leading to the Peach Spring Tuff supereruption, Arizona, Nevada and California, MSc thesis, Vanderbilt University, Nashville, TN.

Cashman, K. V. (1988). Crystallization of Mount St. Helens 1980–1986 dacite—a quantitative textural approach. *Bulletin of Volcanology* **50**, 194–209.

Cashman, K. V. (1992). Groundmass crystallization of Mount St. Helens dacite, 1980–1986—a tool for interpreting shallow magmatic processes. *Contributions to Mineralogy and Petrology* **109**, 431–449.

Cashman, K. V. & Marsh, B. D. (1988). Crystal size distribution (CSD) in rocks and the kinetics and dynamics of crystallization. 2. Makaopuhi Lava Lake. *Contributions to Mineralogy and Petrology* **99**, 292–305.

Chesner, C. A. & Rose, W. I. (1991). Stratigraphy of the Toba Tuffs and the evolution of the Toba Caldera Complex, Sumatra, Indonesia. *Bulletin of Volcanology* **53**, 343–356.

Claiborne, L. L., Miller, C. F., Walker, B. A., Wooden, J. L., Mazdab, F. K. & Bea, F. (2006). Tracking magmatic processes through Zr/Hf ratios in rocks and Hf and Ti zoning in zircons: An example from the Spirit Mountain batholith, Nevada. *Mineralogical Magazine* **70**, 517–543.

Claiborne, L. L., Miller, C. F. & Wooden, J. L. (2010). Trace element composition of igneous zircon: a thermal and compositional record of the accumulation and evolution of a large silicic batholith, Spirit Mountain, Nevada. *Contributions to Mineralogy and Petrology* **160**, 511–531.

Colombini, L. L., Miller, C. F., Gualda, G. A. R., Wooden, J. L. & Miller, J. S. (2011). Titanite and zircon in the Highland Range volcanic sequence (Miocene, southern Nevada, USA): elemental partitioning, phase relations, and influence on evolution of silicic magma. *Mineralogy and Petrology* **102**, 29–50.

Cooper, G. F., Wilson, C. J. N., Millet, M., Baker, J. A. & Smith, E. G. C. (2012). Systematic tapping of independent magma chambers during the 1 Ma Kidnappers supereruption. *Earth and Planetary Science Letters* **313–314**, 23–33.

Cooper, K. M. & Reid, M. R. (2003). Re-examination of crystal ages in recent Mount St. Helens lavas: implications for magma reservoir processes. *Earth and Planetary Science Letters* **213**, 149–167.

Couch, S., Sparks, R. S. J. & Carroll, M. R. (2001). Mineral disequilibrium in lavas explained by convective self-mixing in open magma chambers. *Nature* **411**, 1037–1039.

Crowley, J. L., Schoene, B. & Bowring, S. A. (2007). U–Pb dating of zircon in the Bishop Tuff at the millennial scale. *Geology* **35**, 1123–1126.

Deering, C. D. & Bachmann, O. (2010). Trace element indicators of crystal accumulation in silicic igneous rocks. *Earth and Planetary Science Letters* **297**, 324–331.

Deering, C. D., Bachmann, O. & Vogel, T. A. (2011). The Ammonia Tanks Tuff: Erupting a melt-rich rhyolite cap and its remobilized crystal cumulate. *Earth and Planetary Science Letters* **310**, 518–525.

De Silva, S. L., Self, S., Francis, P. W., Drake, R. E. & Ramirez, C. R. (1994). Effusive silicic volcanism in the Central Andes: The Chao dacite and other young lavas of the Altiplano–Puna Volcanic Complex. *Journal of Geophysical Research* **99**, 17805–17825.

Druitt, T. H. & Bacon, C. R. (1989). Petrology of the zoned calcalkaline magma chamber of Mount Mazama, Crater Lake, Oregon. *Contributions to Mineralogy and Petrology* **101**, 245–259.

Ferguson, C. A. (2008). Silver Creek caldera, probable source of the Miocene Peach Spring Tuff, Oatman Mining District, Arizona. *Geological Society of America, Abstracts with Programs* **40**, 33.

Ferguson, C. A., McIntosh, W. C. & Miller, C. F. (2012). Silver Creek caldera—The tectonically dismembered source of the Peach Spring Tuff. *Geology* **41**, 3–6.

Ferry, J. M. & Watson, E. B. (2007). New thermodynamic models and revised calibrations for the Ti-in-zircon and Zr-in-rutile thermometers. *Contributions to Mineralogy and Petrology* **154**, 429–437.

Gaudio, S. (2003). Discrimination and correlation of the Peach Springs Tuff and Peach Springs age-equivalent ignimbrites by geochronology, petrography, and incompatible element geochemistry from the Northern Colorado River Extensional Corridor, Central Basin and Range Province, USA. B.S. Thesis: College of Wooster, Wooster, OH, 67 p.

Ghiorso, M. S. & Gualda, G. A. R. (2013). A method for estimating the activity of titania in magmatic liquids from the compositions of coexisting rhombohedral and cubic iron–titanium oxides. *Contributions to Mineralogy and Petrology* **165**, 73–81.

Ghiorso, M. S. & Sack, R. O. (1995). Chemical mass transfer in magmatic processes. IV. A revised and internally consistent thermodynamic model for the interpolation and extrapolation of liquid–solid equilibria in magmatic systems at elevated temperatures and pressures. *Contributions to Mineralogy and Petrology* **119**, 197–212.

Glazner, A. F., Nielson, J. E., Howard, K. A. & Miller, D. M. (1986). Correlation of the Peach Springs Tuff, a large-volume Miocene ignimbrite sheet in California and Arizona. *Geology* **14**, 840–843.

Glazner, A. F., Coleman, D. S. & Bartley, J. M. (2008). The tenuous connection between high-silica rhyolites and granodiorite plutons. *Geology* **36**, 183–186.

Gualda, G. A. R. (2007). Crystal and bubble populations in the early-erupted Bishop rhyolitic magma: Microscopy, X-ray tomography and microanalysis of pumice clasts, PhD thesis, University of Chicago, Chicago.

Gualda, G. A. R. & Rivers, M. L. (2006). Quantitative 3D petrography using X-ray tomography: Application to Bishop Tuff pumice clasts. *Journal of Volcanology and Geothermal Research* **154**, 48–62.

Gualda, G. A. R., Cook, D. L., Chopra, R., Qin, L. P., Anderson, A. T., Jr & Rivers, M. L. (2004). Fragmentation, nucleation and migration of crystals and bubbles in the Bishop Tuff rhyolitic magma. *Transactions of the Royal Society of Edinburgh, Earth Sciences* **95**, 375–390.

Gualda, G. A. R., Pamukcu, A. S., Claiborne, L. L. & Rivers, M. L. (2010). Quantitative 3D petrography using X-ray tomography. 3. Documenting accessory phases with differential absorption tomography. *Geosphere* **6**, 782–792.

Gualda, G. A. R., Ghiorso, M. S., Lemons, R. V. & Carley, T. L. (2012*a*). Rhyolite-MELTS: a modified calibration of MELTS optimized for silica-rich, fluid-bearing magmatic systems. *Journal of Petrology* **53**, 875–890.

Gualda, G. A. R., Pamukcu, A. S., Ghiorso, M. S., Anderson, A. T., Sutton, S. R. & Rivers, M. L. (2012*b*). Timescales of quartz crystallization and the longevity of the Bishop giant magma body. *PLoS One* **7**, e37492.

Halliday, A. N., Mahood, G. A., Holden, P., Metz, J. M., Dempster, T. J. & Davidson, J. P. (1989). Evidence for long residence times of rhyolitic magma in the Long Valley magmatic system: the isotopic record in precaldera lavas of Glass Mountain. *Earth and Planetary Science Letters* **94**, 274–290.

Hayden, L. A. & Watson, E. B. (2007). Rutile saturation in hydrous siliceous melts and its bearing on Ti-thermometry of quartz and zircon. *Earth and Planetary Science Letters* **258**, 561–568.

Hayden, L. A., Watson, E. B. & Wark, D. A. (2008). A thermobarometer for titanite (titanite). *Contributions to Mineralogy and Petrology* **155**, 529–540.

Hildreth, W. (1979). The Bishop Tuff: Evidence for the origin of compositional zonation in silicic magma chambers. In: Chapin, C. E. & Elson, W. E. (eds) *Ash-flow Tuffs. Geological Society of America, Special Papers* **180**, 43–75.

Hildreth, W. (1981). Gradients in silicic magma chambers—implications for lithospheric magmatism. *Journal of Geophysical Research* **86**, 153–192.

Hildreth, W. (2004). Volcanological perspectives on Long Valley, Mammoth Mountain, and Mono Craters: several contiguous but discrete systems. *Journal of Volcanology and Geothermal Research* **136**, 169–198.

Hillhouse, J. W. & Wells, R. E. (1991). Magnetic fabric, flow directions, and source area of the lower Miocene Peach Springs Tuff in Arizona, California, and Nevada. *Journal of Geophysical Research* **96**, 12443–12460.

Howard, K. A. & John, B. E. (1987). Crustal extension along a rooted system of imbricate low-angle faults: Colorado River extensional corridor, California and Arizona. In: Coward, M. P., Dewey, J. F. & Hancock, P. L. (eds) *Continental Extensional Tectonics. Geological Society, London, Special Publications* **28**, 299–311.

Huang, R. & Audetat, A. (2012). The titanium-in-quartz (TitaniQ) thermobarometer: A critical examination and re-calibration. *Geochimica et Cosmochimica Acta* **84**, 75–89.

Huber, C., Bachmann, O. & Dufek, J. (2010). The limitations of melting on the reactivation of silicic mushes. *Journal of Volcanology and Geothermal Research* **195**, 97–105.

Jerram, D. A., Cheadle, M. J. & Philpotts, A. R. (2003). Quantifying the building blocks of igneous rocks: Are clustered crystal frameworks the foundation? *Journal of Petrology* **44**, 2033–2051.

Kennedy, B. & Stix, J. (2007). Magmatic processes associated with caldera collapse at Ossipee ring dyke, New Hampshire. *Geological Society of America Bulletin* **119**, 3–17.

Knesel, K. M. & Duffield, W. A. (2007). Gradients in silicic eruptions caused by rapid inputs from above and below rather than protracted chamber differentiation. *Journal of Volcanology and Geothermal Research* **167**, 181–197.

Kuiper, K. F., Deino, A., Hilgen, F. J., Krijgsman, W., Renne, P. R. & Wijbrans, J. R. (2008). Synchronizing rock clocks of Earth history. *Science* **320**, 500–504.

Le Bas, M. J., Le Maitre, R. W., Streckeisen, A. & Zanettin, B. (1986). A chemical classification of volcanic rocks based on the total alkali–silica diagram. *Journal of Petrology* **27**, 745–750.

Linnen, R. L. & Keppler, H. (2002). Melt composition control of Zr/Hf fractionation in magmatic processes. *Geochimica et Cosmochimica Acta* **66**, 3293–3301.

Lipman, P. W., Christiansen, R. L. & O'Connor, J. T. (1966). A compositionally zoned ash-flow sheet in southern Nevada. *US Geological Survey, Professional Paper*, **524-F**.

Macdonald, R. & Belkin, H. E. (2002). Compositional variation in minerals of the chevkinite group. *Mineralogical Magazine* **66**, 1075–1098.

Mangan, M. T. (1990). Crystal size distribution systematics and the determination of magma storage times: The 1959 eruption of Kilauea volcano, Hawaii. *Journal of Volcanology and Geothermal Research* **44**, 295–302.

Marsh, B. D. (1988). Crystal size distribution (CSD) in rocks and the kinetics and dynamics of crystallization. 1. Theory. *Contributions to Mineralogy and Petrology* **99**, 277–291.

Marsh, B. D. (1998). On the interpretation of crystal size distributions in magmatic systems. *Journal of Petrology* **39**, 553–599.

Maughan, L. L., Christansen, E. H., Best, M. G., Gromme, C. S., Deino, A. L. & Tingey, D. G. (2002). The Oligocene Lund Tuff, Great Basin, USA: A very large volume monotonous intermediate. *Journal of Volcanology and Geothermal Research* **113**, 129–157.

Mazdab, F. K. (2009). Characterization of flux-grown trace-element-doped titanite using the high-mass-resolution ion microprobe (SHRIMP-RG). *Canadian Mineralogist* **47**, 813–831.

Mazdab, F. K., Wooden, J. L. & Barth, A. P. (2007). Trace element variability in titanite from diverse geologic environments. *Geological Society of America, Abstracts with Programs* **39**, 406.

McCanta, M. C., Rutherford, M. J. & Hammer, J. E. (2007). Pre-eruptive and syn-eruptive conditions in the Black Butte, California dacite: Insight into crystallization kinetics in a silicic magma system. *Journal of Volcanology and Geothermal Research* **160**, 263–284.

McCracken, R. G., Miller, C. F., Dufek, J., Gualda, G. A. R., Buesch, D. & Brooks, C. E. (2011). Understanding the Peach Spring supereruption through its basal layer deposits (Southwestern USA). *EOS Transactions, American Geophysical Union, Fall Meeting Supplement*, V51F-2572.

Metcalf, R. V. (2004). Volcanic–plutonic links, plutons as magma chambers and crust-mantle interaction: a lithospheric scale view of magma systems. In: Ishihara, S., Stephens, W. E., Harley, S. L., Arima, M. & Nakajima, T. (eds) *The Fifth Hutton Symposium on The Origin of Granites & Related Rocks. Geological Society of America, Special Papers* **389**, 357–374.

Miller, J. S., Heizler, M. T. & Miller, C. F. (1998). Timing of magmatism, basin formation, and tilting at the west edge of the Colorado River Extensional Corridor: Results from single-crystal $^{40}Ar/^{39}Ar$ geochronology of Tertiary rocks in the Old Woman Mountains Area, Southeastern California. *Journal of Geology* **106**, 195–209.

Nielson, J. E., Lux, D. R., Dalrymple, G. B. & Glazner, A. F. (1990). Age of the Peach Springs Tuff, Southeastern California and Western Arizona. *Journal of Geophysical Research* **95**, 571–580.

Pallister, J. S., Hoblitt, R. P. & Reyes, A. G. (1992). A basalt trigger for the 1991 eruptions of Pinatubo volcano? *Nature* **356**, 426–428.

Pamukcu, A. S. & Gualda, G. A. R. (2010). Quantitative 3D petrography using X-ray tomography. 2. Combining information at various resolutions. *Geosphere* **6**, 775–781.

Pamukcu, A. S., Gualda, G. A. R. & Anderson, A. T., Jr (2012). Crystallization stages of the Bishop Tuff magma body recorded in crystal textures in pumice clasts. *Journal of Petrology* **53**, 589–609, doi:10.1093/petrology/egr072.

Pearthree, P. A. (2007). *Geologic map of the Needles NE 7½' Quadrangle, Mohave County, Arizona. Arizona Geological Survey Digital Geologic Map DGM-53* .

Pearthree, P. A., Ferguson, C. A., Johnson, B. J. & Guynn, J. (2009). *Geologic map and report for the proposed State Route 95 Realignment Corridor, Mohave County, Arizona, version 1.0. Arizona Geological Survey Digital Geologic Map DGM-65* .

Reid, M. R. (2008). How long does it take to supersize an eruption? *Elements* **4**, 23–28.

Schmitt, A. K., Danisik, M., Evans, N. J., Siebel, W., Kiemele, E., Aydin, F. & Harvey, J. C. (2011). Acigol rhyolite field, Central Anatolia (part 1): High-resolution dating of eruption episodes and zircon growth rates. *Contributions to Mineralogy and Petrology* **162**, 1215–1231.

Sherrod, D. R. & Nielson, J. E. (eds) (1993). *Tertiary stratigraphy of highly extended terranes, California, Arizona, Nevada. US Geological Survey Bulletin* **2053**.

Simon, J. I. & Reid, M. R. (2005). The pace of rhyolite differentiation and storage in an 'archetypical' silicic magma system, Long Valley, California. *Earth and Planetary Science Letters* **235**, 123–140.

Sisson, T. W. & Bacon, C. R. (1999). Gas-driven filter pressing in magmas. *Geology* **27**, 613–616.

Smith, R. L. (1960). Ash flows. *Geological Society of America Bulletin* **71**, 795–841.

Smith, R. L. (1979). Ash flow magmatism. In: Chapin, C. E. & Elston, W. E. (eds) *Ash-flow Tuffs. Geological Society of America, Special Papers* **180**, 5–27.

Smith, R. L. & Bailey, R. A. (1966). The Bandelier Tuff: A study of ash-flow eruption cycles from zoned magma chambers. *Bulletin Volcanologique* **29**, 83–104.

Sparks, S. R. J., Sigurdsson, H. & Wilson, L. (1977). Magma mixing-mechanism for triggering acid explosive eruptions. *Nature* **5609**, 315–318.

Thorson, J. P. (1971). Igneous petrology of the Oatman District, Mojave County, Arizona, PhD thesis, University of California, Santa Barbara.

Valentine, G. A., Buesch, D. C. & Fisher, R. V. (1989). Basal layered deposits of the Peach Springs Tuff, northwestern Arizona, USA. *Bulletin of Volcanology* **51**, 395–414.

Valentine, G. A., Buesch, D. C. & Fisher, R. V. (1990). Reply to Wilson and Self's comments on: Basal layered deposits of the Peach Springs Tuff, northwestern Arizona, USA. *Bulletin of Volcanology* **52**, 565–569.

Varga, R. J., Faulds, J. E., Snee, L. W., Harlan, S. S. & Bettison-Varga, L. (2004). Miocene extension and extensional folding in an

anticlinal segment of the Black Mountains accommodation zone, Colorado River extensional corridor, southwestern United States. *Tectonics* **23**, TC1019, doi:10.1029/2002TC001454.

Vazquez, J. A. & Reid, M. R. (2004). Probing the accumulation history of the voluminous Toba magma. *Science* **305**, 991–994.

Wark, D. A. & Miller, C. F. (2008). Supervolcanoes and their explosive supereruptions. *Elements* **4**, 11–15.

Wark, D. A., Hildreth, W., Spear, F. S., Cherniak, D. J. & Watson, E. B. (2007). Pre-eruption recharge of the Bishop magma system. *Geology* **35**, 235–238.

Watson, E. B. (1996). Dissolution, growth and survival of zircons during crustal fusion: Kinetic principles, geological models and implications for isotopic inheritance. *Transactions of the Royal Society of Edinburgh, Earth Sciences* **87**, 43–56.

Watson, E. B. & Harrison, T. M. (1983). Zircon saturation revisited: temperature and composition effects in a variety of crustal magma types. *Earth and Planetary Science Letters* **64**, 295–304.

Wells, R. E. & Hillhouse, J. W. (1989). Paleomagnetism and tectonic rotation of the lower Miocene Peach Spring Tuff: Colorado Plateau, Arizona, to Barstow, California. *Geological Society of America Bulletin* **101**, 846–863.

Wilson, C. J. N. & Self, S. (1990). Comment on: Basal layered deposits of the Peach Springs Tuff, northwestern Arizona, USA. *Bulletin of Volcanology* **52**, 562–564.

Young, R. A. & Brennan, W.J. (1974). Peach Springs Tuff: Its bearing on structural evolution of the Colorado Plateau and development of Cenozoic drainage in Mohave County, Arizona. *Geological Society of America Bulletin* **83**, 83–90.